Durham E-Theses

Absorption Spectroscopy of a K+Cs Mixture Cell and Simulation of Time-Averaged Optical Potentials

KATO, AYUMI

How to cite:

Use policy

Absorption Spectroscopy of a K+Cs Mixture Cell and Simulation of Time-Averaged Optical Potentials

Ayumi Kato

A thesis submitted in fulfilment
of the requirements for the degree of
Master of Science by Research

Durham University

Department of Physics
December 16, 2015

Absorption Spectroscopy of a K+Cs Mixture Cell and Simulation of Time-Averaged Optical Potentials

Ayumi Kato

Abstract

In the first part of the report, Doppler-broadened absorption spectroscopy was performed on a natural abundance K+Cs mixture species cell to determine whether interspecies molecular transitions are observable at sufficiently high vapour pressures. It was found that the cell behaves independently of the presence of the other alkali metal for spectroscopy on both the Cs D2 and K D2 lines for a temperature range between 27.8 °C - 45.4 °C, and 34.8 °C - 150 °C, respectively. Above the temperature of 155 °C, the spectroscopic signal on the K D2 line exhibits absorption features which is potentially the result of rotational transitions in the K_2 molecule, however, this is not definitive and further investigations are needed to confirm this.

In the second part, we developed and tested several codes on a MATLAB program to simulate time-averaged potentials using an acousto-optic modulator (AOM). We demonstrated three different coding methods to generate smooth trapping potentials and characterised different parameters required to accomplish such a potential. We also investigated the depth of the trapping potential of a harmonic potential and the requirements to accurately approximate the trap frequencies.

Declaration

I confirm that no part of the material offered has previously been submitted by myself for a degree in this or any other University. Where material has been generated through joint work, the work of others has been indicated.

Ayumi Kato
Durham, December 16, 2015

Acknowledgements

I would like to thank my supervisor, Prof. Simon Cornish and Dr. Ana Rakonjac for their guidance and supervision throughout the past year.

Contents

Chapter 1

Introduction

1.1 Motivation

This report is divided into two parts: absorption spectroscopy and the simulation of time-averaged potentials. Absorption spectroscopy is performed on a mixed species vapour cell containing potassium and cesium to determine whether the absorption spectra for the individual elements are affected by the presence of a different species within the same cell. The motivation for using a mixed species cell is to establish whether interspecies molecular transitions are observable in such a cell at sufficiently high vapour pressures. Spectroscopy of single alkali species has been subject to extensive studies, especially for rubidium and cesium [1], however mixed alkali species have not been extensively studied.

Part 2 of the report discusses a MATLAB simulation of time-averaged optical dipole force potentials created using acousto-optic modulators (AOMs). AOMs provide a way of confining Bose-Einstein condensates (BECs) in arbitrary trapping potentials and have been demonstrated to realise various trapping geometries such as toroids, ring lattices [2], and optical box trapping geometries [3] which has led to a wide range of fundamental research in areas such as superfluidity [4] and matter-wave interferometry [4, 5]. These trapping potentials are achieved by exploiting the optical dipole interaction which relies on the atomic dipole moment and an appropriate laser field intensity. Experimentally, the optical potentials are linearly proportional to the laser intensity. One of the key requirements for successfully trapping BECs in an arbitrary trapping potential is a smooth trapping potential to minimise heating of the trapped particles [5]. The aim of the simulation is to extract useful parameters for use in experiments invovlving trapping BECs, such as the rate of modulation required for the creation of smooth trapping potentials and accurate approximation of frequencies of harmonic trapping potentials.

1.2 Report Layout

Part 1 of the report begins by introducing the background concepts behind Doppler-broadened and absorption spectroscopy. In chapter 3, the experimental setup and the workings of the extended cavity diode lasers is detailed. This chapter also includes the signal resulting from the Doppler-broadened spectroscopy of a single species cell of potassium and cesium for comparison to the Doppler-broadened signal from a mixed species cell. The results from the Doppler-broadened spectroscopy of the mixed species cell for cesium and potassium are included in chapter 4.

Part 2 of the report concerns the simulation of time-averaged potentials. A brief introduction on the construct of an AOM and a theoretical background of optical dipole traps are given in chapter 5. The codes that were developed on MATLAB to simulate time-averaged potentials are presented and the parameters required to simulate a sufficiently smooth potential with a low RMS error are determined in chapter 6. The results characterising the trap depth variation and trapping frequencies are presented in chapter 7.

Part I

Absorption Spectroscopy

Chapter 2

Absorption Spectroscopy of a K+Cs Mixture Cell

2.1 Theory of a Two Level Atom

One of the techniques of laser spectroscopy of atomic vapours involves sending monochromatic laser light of known intensity through a sample of atomic or molecular gas and then measuring the intensity of light exiting the cell, with the ratio of the two intensities giving the transmission. The laser frequency is then swept across a desired range producing a spectrum of transmission as a function of frequency. The frequencies at which the laser light becomes resonant with a particular transition manifest as dips in the transmission spectrum [6].

The advantages of laser spectroscopy can broadly be characterized by comparing it to older spectrophotometric methods. Conventional spectroscopy typically involves a broad-spectrum light source (atomic vapour lamps, fluorescent light bulbs) that is then spectrally filtered using a monochromator (usually diffraction grating with supporting optics) so that the sample is illuminated by a narrow range of frequencies [6]. The resolution, however, is limited by two factors: Doppler broadening of the atomic transitions due to the velocity distribution of atoms in the vapour and due to the resolving power of the monochromator. The resolving power, or resolvance is simply the ratio of the wavelength to the smallest resolvable wavelength interval. Most modern commercial spectrophotometers have a resolvance between 10^4 -10^5, whereas with Fabry-Perot cavities of free spectral range (FSR) on the order of 100 MHz, the resolvance improves to between 10^5-10^6. As detailed later, laser spectroscopy can also be set up in such a way as to eliminate Doppler broadening. Altogether, laser spectroscopy paves the way for the most precise measurements of atomic spectral features.

The spectroscopic method used in this experiment operates in the weak probe regime. The idea behind this technique is that the most accurate transmission spectra are obtained when the laser power is low enough such that the ground state population of the atoms is not changed significantly. When an electron is excited to a higher energy state, it remains there for roughly the lifetime of that particular state, before decaying back down. While the atom is thus excited, it appears effectively invisible to the incoming photons since they are no longer in resonance with any transition. If the rate of photons incident on the atom is larger than the lifetime, there will be a fraction of photons that will pass through unimpeded. The effect of this on experimental results is to effectively decrease the signal to noise ratio of the spectrum.

In order to put this on a more quantitative basis, the optical Bloch equations for a two level atom interacting with an external laser field are solved. The derivations in this chapter follow the treatment in Refs. [7–9].

The Hamiltonian of the system is:

$$H = H_A + H_I(t), \qquad (2.1)$$

where H_A corresponds to the atomic part of the Hamiltonian and $H_I(t)$ to the time dependent interaction with the laser field. The solution in the absence of the interaction term is simple and is given in terms of the atomic eigenvectors and an explicit time dependence factored out:

$$\psi(\mathbf{r}, t) = c_1(t)|1\rangle e^{-i\omega_1 t} + c_2(t)|2\rangle e^{-i\omega_2 t}, \qquad (2.2)$$

where $\omega_n = E_n/\hbar$ and E_n are the energy eigenvalues for the atomic Hamiltonian: $H_A|n\rangle = E_n|n\rangle$. Since this is a closed two level system, the coefficients also obey $|c_1(t)|^2 + |c_2(t)|^2 = 1$ where c_1 and c_2 are the complex amplitudes of the wavefunction. The light field can now be included in the calculation. In the dipole approximation, the Hamiltonian is given as:

$$H_I = -\mathbf{D} \cdot \mathbf{E} \cos(\omega_L t). \qquad (2.3)$$

Here, $\mathbf{E}\cos(\omega_L t)$ corresponds to the classical electric field of a monochromatic light field with frequency ω_L and $\mathbf{D} = e\mathbf{r}$ is the electric dipole term for a single electron of charge e at a position $\mathbf{r}$ from the atoms centre of mass. The dipole approximation can be assumed to hold for the consideration of alkali atoms since they only have a single valence electron and the wavelength of the incident light is much larger than the atomic radius. Substituting

equation (2.2) into the time dependent Schrödinger equation yields a coupled set of time dependent equations for the coefficients:

$$i\dot{c}_1(t) = \Omega\cos(\omega_L t)e^{-i\omega_0 t}c_2(t) \tag{2.4}$$

$$i\dot{c}_2(t) = \Omega\cos(\omega_L t)e^{i\omega_0 t}c_1(t), \tag{2.5}$$

with $\omega_0 = \omega_2 - \omega_1$ and also having defined the Rabi frequency, representing the rate of population fluctuation between the two levels, as:

$$\Omega = -\frac{\langle 1|e\mathbf{r}\cdot\mathbf{E}|2\rangle}{\hbar}. \tag{2.6}$$

Now equations (2.4) and (2.5) can be expanded to:

$$i\dot{c}_1(t) = \frac{\Omega}{2}[e^{i(\omega_L-\omega_0)t} + e^{-i(\omega_0+\omega_L)t}]c_2(t) \tag{2.7}$$

$$i\dot{c}_2(t) = \frac{\Omega}{2}[e^{i(\omega_0+\omega_L)t} + e^{i(\omega_0-\omega_L)t}]c_1(t). \tag{2.8}$$

Next, the rotating wave approximation is made, which eliminates the fast oscillating terms containing $\omega_0 + \omega_L$ since they are much faster than the other two terms and over the interaction time, average out to a null contribution. This gives us the following coupled equations:

$$i\dot{c}_1(t) = \Omega e^{i(\omega_L-\omega_0)t}c_2(t) \tag{2.9}$$

$$i\dot{c}_2(t) = \Omega e^{i(\omega_0-\omega_L)t}c_1(t). \tag{2.10}$$

Using these equations, a density matrix for the system can be defined:

$$\rho = \begin{pmatrix} \rho_{11} & \rho_{12} \\ \rho_{21} & \rho_{22} \end{pmatrix} = \begin{pmatrix} |c_1|^2 & c_1 c_2^* \\ c_1^* c_2 & |c_2|^2 \end{pmatrix}, \tag{2.11}$$

where the time dependence in front of the coefficients has been dropped for brevity. The use of this matrix is that it gives us useful information in a compact notation; the diagonal terms correspond to the occupation probability of the two states, whereas the off-diagonal terms account for any coherences that exist between the two states. The matrix must have a trace equal to one and must also be Hermitian, giving $\rho_{21} = \rho_{12}^*$. The final thing left to consider is the inclusion of spontaneous emission, which is impossible to derive from semi-classical theory. Instead a factor Γ_0 modeling spontaneous emission as a loss of coherence in the off diagonal elements is included:

$$\dot{\rho}_{21}^{\text{spon}} = -\frac{\Gamma_0}{2}\rho_{21}, \tag{2.12}$$

with Γ_0 calculated from Fermis Golden Rule requiring quantisation of the field modes of the incident light:

$$\Gamma_0 = \frac{\omega^3|\langle 1|r|2\rangle|^2}{3\pi\epsilon_0^3}. \tag{2.13}$$

The lifetime of the excited state can be defined as $\tau = 1/\Gamma_0$. In this treatment, any effects of collisions are excluded, which would serve to reduce the lifetime. The optical Bloch equations can now be written, where the laser detuning from the transition is introduced $\Delta = \omega_{\text{L}} - \omega_0$ and taking the exponential time dependence into $\tilde{\rho}_{21} = \rho_{21}e^{i\omega_L t}$, $\tilde{\rho}_{12} = \rho_{12}e^{-i\omega_L t}$:

$$\dot{\rho}_{22} = -\Gamma_0\rho_{22} + i\frac{\Omega}{2}(\tilde{\rho}_{21} - \tilde{\rho}_{12}), \tag{2.14}$$

$$\dot{\rho}_{11} = \Gamma_0\rho_{22} + i\frac{\Omega}{2}(\tilde{\rho}_{12} - \tilde{\rho}_{21}), \tag{2.15}$$

$$\dot{\tilde{\rho}}_{12} = -\left(\frac{\Gamma_0}{2} + i\Delta\right)\rho_{12} + i\frac{\Omega}{2}(\rho_{11} - \rho_{22}). \tag{2.16}$$

In the steady state, all the above equations are equal to zero. To obtain the excited state probability we substitute ρ_{12} and $\rho_{21} = \rho_{12}^*$ from equation (2.16) into equation (2.14). We also make the substitution $\rho_{11} = 1 - \rho_{22}$, yielding:

$$\rho_{22} = \frac{\Omega^2}{\Gamma_0^2 + 4\Delta^2 + 2\Omega^2}. \tag{2.17}$$

To obtain the final scattering rate, equation (2.17) is multiplied by Γ_0 to obtain:

$$R_{\text{scatt}} = \frac{\Gamma_0}{2}\frac{\Omega^2/2}{\Gamma_0^2/4 + \Delta^2 + \Omega^2/2}. \tag{2.18}$$

From this equation, it is evident that no matter how high the Rabi frequency and hence electric field strength become, the scattering rate will tend to $\Gamma_0/2$, meaning that the atom is scattering at half its decay rate. This is easy to understand because in the same limit, $\rho_{11}/\rho_{22} = 1$, and the atom spends equal amounts of time in the ground and excited state. It is therefore useful to define a saturation parameter in terms of the laser intensity I and saturation intensity I_{sat}, which is a more directly tangible physical quantity in the laboratory:

$$\frac{I}{I_{\text{sat}}} = 2\frac{\Omega^2}{\Gamma_0^2}, \tag{2.19}$$

giving a redefined scattering rate:

$$R_{\text{scatt}} = \frac{\Gamma_0}{2}\frac{I/I_{\text{sat}}}{1 + I/I_{\text{sat}} + 4\Delta^2/\Gamma_0^2}, \tag{2.20}$$

and occupation ratio:

$$\frac{\rho_{11}}{\rho_{22}} = \frac{I/I_{\text{sat}}}{2 + I/I_{\text{sat}} + 8\Delta^2/\Gamma_0^2}. \tag{2.21}$$

Thus to be in the weak probe regime, the condition $I \ll I_{\text{sat}}$ is required. The saturation intensity can be calculated as the ratio of the incident photon energy to the cross-section $3\lambda^2/\pi$ times the state lifetime to give:

$$I_{\text{sat}} = \frac{\hbar\pi\omega_0}{3\lambda^2\tau} = \frac{2\hbar\pi^2 c}{3\lambda^2\tau}. \tag{2.22}$$

From this, the saturation intensity for the species used in this experiment can be calculated, giving $I_{\text{sat}} = 2.71$ mW/cm^2 for cesium and $I_{\text{sat}} = 1.75$ mW/cm^2 for potassium, using the values from Appendix A.

2.2   Doppler Broadening

The simplest possible spectroscopy method involves optically exciting an atomic sample with only a single weak probe beam at resonance (Fig. 2.1). The main contribution to the finite linewidth in probe-only spectroscopy is the Doppler-broadening from the beam exciting atoms of different velocity groups, resulting in a Gaussian line shape. A simple derivation can be used to demonstrate this. The atoms see the laser photons at a new frequency ν_{dop} given by:

$$\nu_{\text{dop}} = \nu_L\left(1 + \frac{v}{c}\right), \tag{2.23}$$

where v is the component of the atom's velocity in the direction of the probe beam. The probability of an atom in the ensemble having a velocity between v and $v + dv$ is given by the Maxwell distribution:

$$P(v)\mathrm{d}v = \left(\frac{M}{2\pi k_{\text{B}}T}\right)^{1/2}\exp\left(-\frac{Mv^2}{2k_{\text{B}}T}\right)\mathrm{d}v, \tag{2.24}$$

where M is the atomic mass, k_{B} is the Boltzmann constant, T is the absolute temperature. From equation (2.23) we see that $\mathrm{d}v = \frac{c}{\nu_{\text{dop}}}\mathrm{d}\nu_L$ and we can thus substitute into

equation (2.24) to obtain the probability of the a laser-atom resonance:

$$P(\nu_L)\mathrm{d}\nu_L = \frac{2}{\delta\pi^{1/2}} \exp \frac{-4(\nu_L - \nu_0)^2}{\delta^2}\mathrm{d}\nu_L, \tag{2.25}$$

where we defined a parameter related to the linewidth $\delta = 2(\nu_0/c)(2k_\mathrm{B}T/M)^{1/2}$. The FWHM gives the linewidth of the Gaussian lineshape, and is shown in 2.2:

$$\mathrm{FWHM} = \delta(\ln 2)^{1/2} = 2\frac{\nu_0}{c}\left(\frac{2k_\mathrm{B}T\ln 2}{M}\right)^{1/2}. \tag{2.26}$$

2.3 Electric Susceptibility

In describing the atom-light interaction of a two level atom using the optical Bloch equations, the treatment so far has been for individual atoms. The susceptibility is used to characterise the collective absorptive and dispersive properties of an ensemble of atoms illuminated with a light field.

The response of a dielectric material to an applied external field (as in equation (2.3)) along one dimension is given by:

$$P = \epsilon_0\chi_0(\Delta)E_0\cos(\omega t) = \frac{1}{2}\epsilon_0 E_0[\chi^*(\Delta)e^{i\omega t} + \chi(\Delta)e^{-i\omega t}], \tag{2.27}$$

where ϵ_0 is the electric permittivity and $\chi_0(\Delta)$ is the electric susceptibility that is a function of the detuning frequency.

To connect this macroscopic response to the two level atom, we use another definition that treats the polarisibility as the product of N atoms and the expectation of their dipole moments $\langle\hat{\mu}\rangle$. Since an atom cannot absorb or emit a photon and remain in the same state, the dipole matrix takes a simple form:

$$\hat{\mu} = \begin{pmatrix} 0 & \mu_{12} \\ \mu_{21} & 0 \end{pmatrix}, \tag{2.28}$$

where the dipole is $\mu = \mu_{12} = \mu_{21} = -\hbar\Omega/E_0$. We make use of the properties of the density matrix to write:

$$P = N\mathrm{Tr}(\hat{\rho}\hat{\mu}) = N\mu(\rho_{12} + \rho_{21}). \tag{2.29}$$

We can once again re-express these variables with the explicit time dependence taken out to obtain:

$$P = N\mu(\tilde{\rho}_{12}e^{i\omega t} + \tilde{\rho}_{21}e^{-i\omega t}). \tag{2.30}$$

Now we can simply compare the coefficient in front of $e^{-i\omega t}$ of this equation to that of equation (2.27) and read off the form of the susceptibility:

$$\chi(\Delta) = \frac{2N\mu}{E_0\epsilon_0}\tilde{\rho}_{21}. \tag{2.31}$$

We can obtain an expression for the coherence term $\tilde{\rho}_{21}$ in the steady state from equation (2.16). Once again, the time derivative $\dot{\tilde{\rho}}_{21}$ must equal zero and furthermore, we can make the assumption that in the limit of weak (infrequent) excitation the majority of the population will be in the ground state, hence $\rho_{11} = 1$ and $\rho_{22} = 0$. Substituting into equation (2.31), whilst also substituting for the Rabi frequency, we obtain:

$$\chi(\Delta) = -\frac{N\mu^2}{\hbar\epsilon_0}\frac{1}{\Delta + i\Gamma_0/2} = -\frac{N\mu^2}{\hbar\epsilon_0}f_{\Gamma_0}(\Delta). \tag{2.32}$$

Here, a lineshape factor $f_{\Gamma_0}(\Delta)$ is introduced. The real and imaginary components of this complex equation are:

$$\chi_{\mathrm{R}}(\Delta) = -\frac{N\mu^2}{\hbar\epsilon_0}\frac{\Delta}{\Delta^2 + \Gamma_0^2/4} \tag{2.33}$$

$$\chi_{\mathrm{Im}}(\Delta) = \frac{N\mu^2}{\hbar\epsilon_0}\frac{\Gamma_0/2}{\Delta^2 + \Gamma_0^2/4}. \tag{2.34}$$

The imaginary part of equation gives a Lorentzian lineshape whereas the real part gives a dispersion curve. The FWHM of the Lorentzian is simply the natural linewidth Γ_0 described earlier with an associated lifetime $\Gamma_0 = 1/\tau$. For cesium and potassium, this is $\Gamma_0 = 2\pi \times 5.23$ MHz [10] and $\Gamma_0 = 2\pi \times 6.04$ MHz [11], respectively.

We can gain further insight into the behaviour of equations (2.33) and (2.34), by first noting the defintion of $\mu^2 = 3\pi\hbar\epsilon_0\Gamma_0^{-3}$ and then defining a dimensionless parameter $a=\Delta/\Gamma_0$. Taking all the constants in front of the fraction into χ_0, equations (2.33) and (2.34) are now re-expressed and plotted in figure 2.1:

$$\chi_R(s) = -\chi_0\frac{a}{2a^2 + 1/2} \tag{2.35}$$

$$\chi_I(s) = \chi_0\frac{1}{4a^2 + 1}. \tag{2.36}$$

It is clear from this plot that at frequencies far from the central detuning i.e., $a \gg 1$, the contribution from the Lorentzian linewidth is much smaller such that $\chi_{\mathrm{Re}} \propto 1/\Delta$ and $\chi_{\mathrm{Im}} \propto 1/\Delta^2$. Hence far from resonance, the dispersion effects dominate over the absorption.

The analysis of electric susceptibility up to now neglected the Doppler broadening effects of atomic motion in a vapour as described in section 2.2. So far, the lineshape used in equation (2.32) was Lorentzian corresponding only to homogenous broadening. The inhomogenous Doppler broadening can be incorporated by taking a convolution of
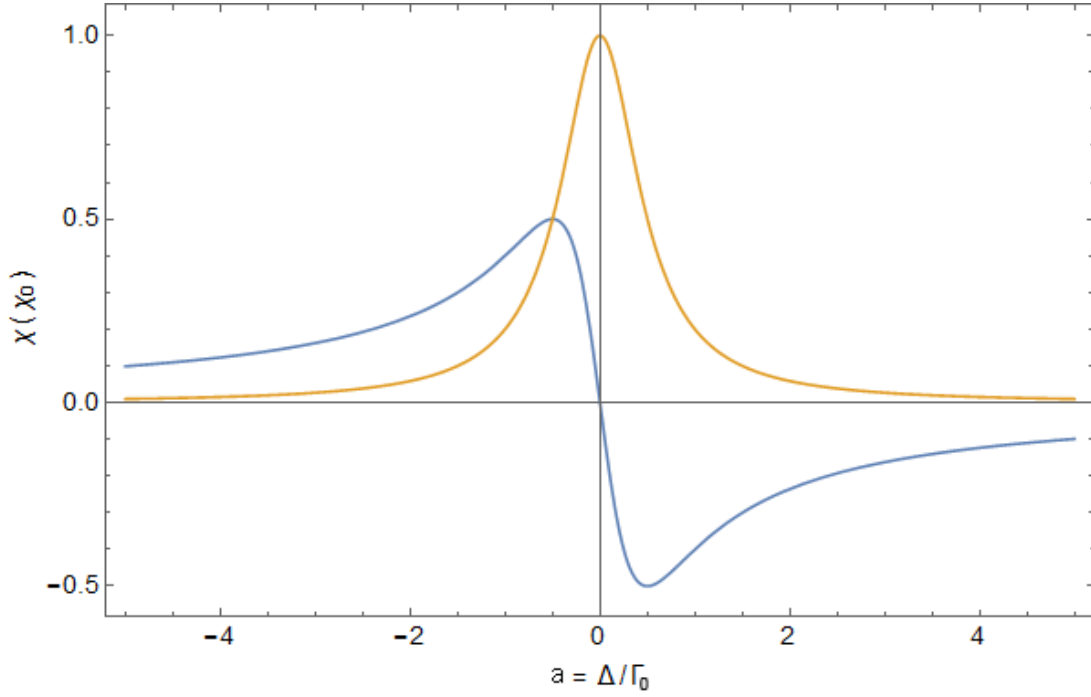
Figure 2.1: Plot of the real and imaginary components of susceptibility for a two-level system for an ensemble of atoms. The blue line indicates the real part and the orange line indicates the imaginary part.

the Lorentzian lineshape shifted by kv in frequency and the Gaussian distribution from equation (2.24) to give the Voigt lineshape s:

$$s(\Delta) = \int_{-\infty}^{+\infty} f_{\Gamma_0}(\Delta - kv) \times P(v) \mathrm{d}v. \qquad (2.37)$$

This lineshape can be used in a model for calculating the line-strength of a particular atomic transition.

2.4   Fitting Routine

Experimentally, the spectra for different temperatures are fitted using Elecsus, a Python program developed by the Atomic and Molecular physics group at Durham University [12]. The program simulates a single weak probe beam described in section 2.2 by calculating the electric susceptibility of a number of alkali vapours which is used for predicting its absorptive and dispersive properties. This is used for calculating the lineshapes of transitions in the Doppler-broadened transmission spectrum of alkali metals, including cesium and potassium. The frequencies and strengths of the spectral features are obtained by numerically solving the full atomic Hamiltonian.

The program can calculate the theoretical transmission lines of the alkali metal set by

the user in the Elecsus program. It can also perform fits to the experimental data that is inputted into the code in the form of a two column .csv file, with the first column giving the linear detuning and the second column containing the transmission data of the spectrum. There are three options for the fitting routine which can be performed on the raw inputted data, and the type of fitting should be selected depending on the number of user-defined parameters. The type of fitting used throughout the report is the Marquardt-Levenberg (ML) method which is the simplest of the available fitting options and works by finding the minimum of the sum of the square deviations [13].

User specified parameters used for the fitting routine include the cell length and the temperature of the cell determined in the method described in the following chapter. Elecsus accepts a cell temperature range between 25 °C and 277 °C.

2.5   K D2 and Cs D2 Lines

The D2 transitions of potassium and cesium are considered in this report since these are used commonly for laser-cooling experiments [1]. The D lines for alkali metals have the highest emission/absorption probability of the optical transitions due to them having the highest oscillator strength.

The transition wavelengths of the D2 lines for cesium and potassium are 852.347 nm $(^2S_{3/2} \rightarrow {}^2P_{3/2})$ and 766.701 nm $(^2S_{1/2} \rightarrow {}^2P_{3/2})$, respectively. Figures 2.2 and 2.3 show the standard energy level diagrams for the D2 lines of potassium and cesium and the relevant properties of the K and Cs D2 lines are found in Appendix A.

^{133}Cs is the only stable, naturally occurring isotope of cesium. The ground state of cesium is split into $F = 3$ and $F = 4$ from the hyperfine interaction between the nuclear magnetic moment and the magnetic field generated by the electron. The transitions from the ground state to the upper excited states is determined by the selection rule $\Delta F = \pm 1, 0$.

There are three naturally occurring isotopes for potassium: ^{39}K,^{40}K and ^{41}K. ^{39}K is most abundant at 93.26%, and ^{40}K is the least abundant isotope accounting for 0.0001% [11].
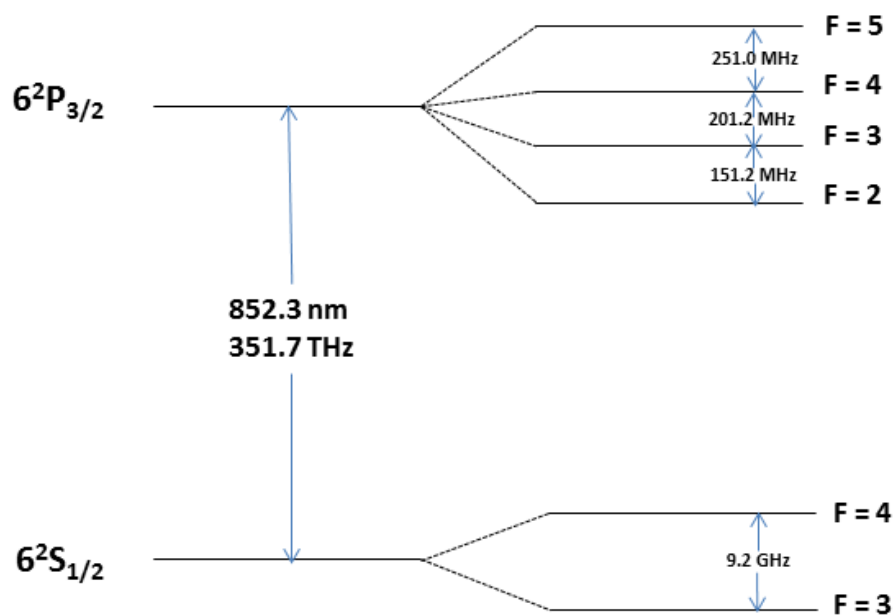
Figure 2.2: D2 energy level diagram of cesium. Note that the figure is not drawn to scale. Values are taken from [10].
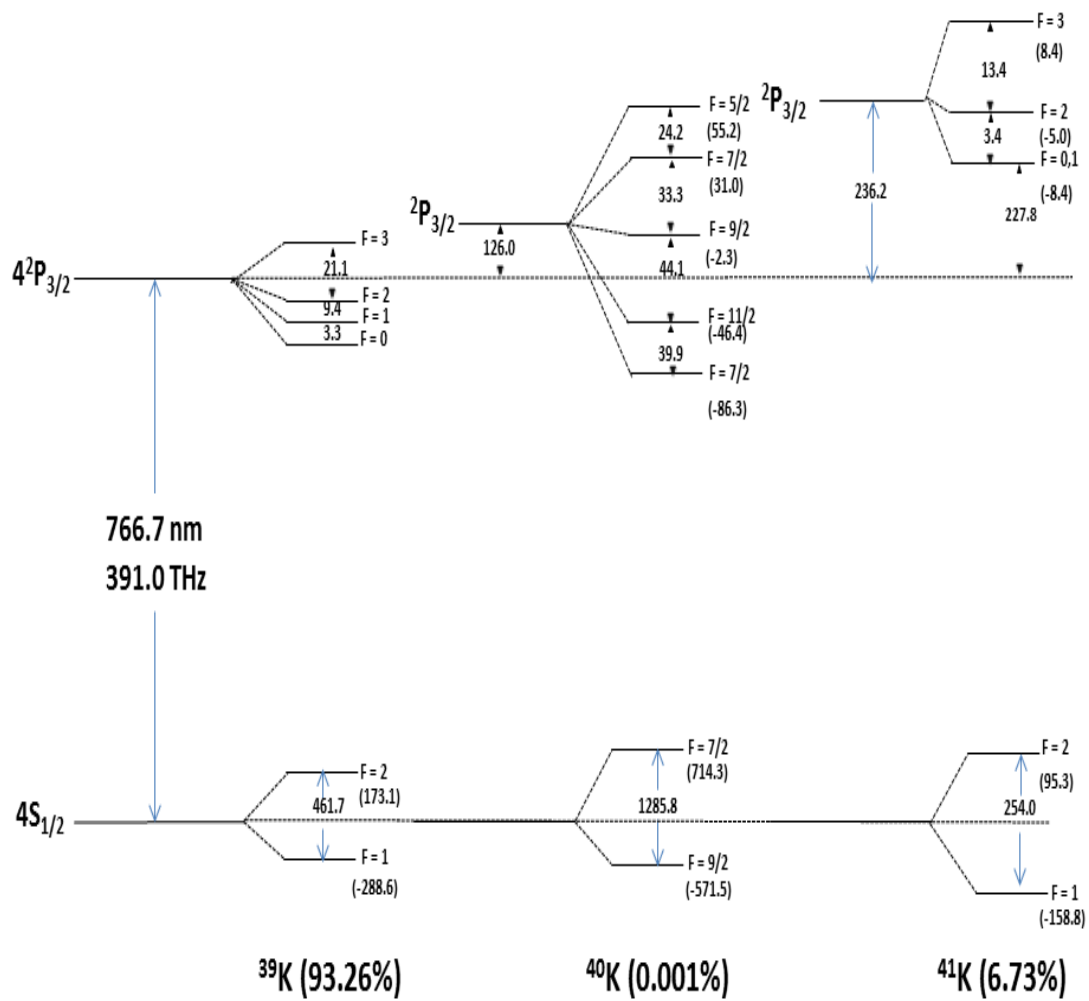
Figure 2.3: D2 energy level diagram of natural abundance potassium. All units for the hyperfine transitions are in MHz. Note that the figure is not drawn to scale. Values are taken from [11].

Chapter 3

Experimental Setup

3.1 General Overview

This section details the experimental setup for Doppler broadened spectroscopy of the D2 lines for the K+Cs mixed species vapour cell. External cavity diode lasers (ECDLs) in the Littrow configuration are used to access the D2 lines of potassium and cesium for the mixture cell. A Fabry-Perot interferometer (FPI) with a free-spectral range (FSR) of 300 MHz is used to calibrate the frequency scale.

3.1.1 ECDLs

Tunable diode lasers are used widely in atomic physics experiments. Some of the main features of ECDLs are briefly covered here since they are extensively used for the experiment. An ECDL uses an adjustable external diffraction grating to form a resonant cavity between itself and the rear facet of a laser diode. A lens which is anti-reflection (AR) coated collimates the light onto an adjustable grating for precise wavelength tuning to the desired atomic transition.

The external cavity in the Littrow confguration is used in this project. In this configuration, the laser diode emits the light onto a grating, which selects the zero order light to be outcoupled to the experiment and the first order light to be reflected back into the diode for feedback. Because the first order beam is reflected, greater optical power can be fed into to the experiment, providing an advantage over the Littman-Metcalf configuration which is the other common external cavity configuration.

Although the extended cavity provides a certain degree of frequency stabilisation with its internal feedback, it does not completely eliminate undesirable effects such as frequency

drifting which can only be accomplished through stabilising the laser frequency with an external feedback mechanism.

3.1.2 K+Cs Mixture Cell

The custom-made K+Cs mixture cell has an optical path length of 1 cm and contains natural abundance potassium and cesium filled at a 1:1 ratio (see Appendix A for their properties). The reason for the short optical path length of the cell is to induce a large number of interatomic collisions at high temperatures to observe any features as a result of the cesium species. The cell is made from pyrex, which is commonly used in spectroscopic experiments and is enclosed in a brass casing and mounted on an aluminium stand as shown in Fig. 3.1. The brass enclosure has an aperture with a radius of .25 cm for optical access.
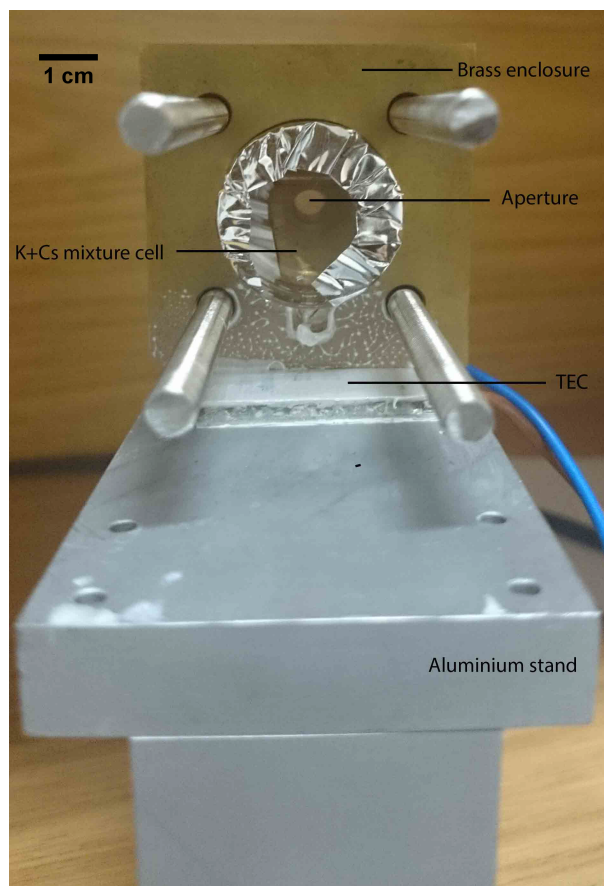
**Figure 3.1:** Cross-sectional image of mixture cell enclosed in a brass casing and placed on a TEC for temperature adjustment and mounted on an aluminium stand.

For temperatures up to 138 °C, the cell is heated using a thermoelectric cooler (TEC) with the hot side in contact with the base of the brass casing. The temperature of the cell is measured using an AD590 transducer placed in a drilled hole with thermal paste

for contact on the side of the casing. The transducer has a linear current response to temperature. The transducer is powered using a 12 V DC supply and the temperature is inferred by measuring the voltage across a 1.00 $\pm$0.05kΩ resistor. The schematic of the circuit used is shown in Fig. 3.2. The transducer has an absolute temperature response of 1 mV/K, giving very accurate temperature readings up to 150 °C.
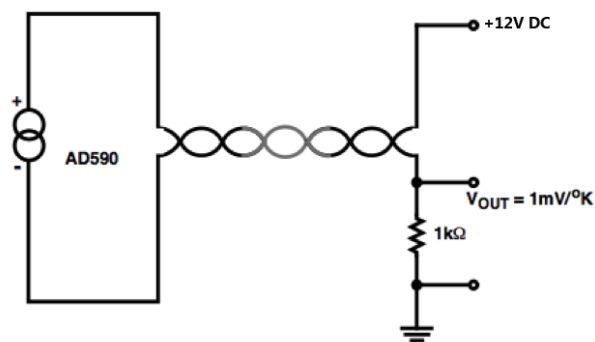
Figure 3.2: Schematic of cell temperature measurement setup using the AD590 transducer. The circuit is powered by a 12 V DC supply, giving an absolute temperature reading of 1 mV/K, measured using a multimeter across the 1.00 $\pm$0.05kΩ resistor. (Edited and adapted from the AD590 specification sheet)

To observe the K D2 line, the cell is heated to a higher temperature compared to the cell temperature when observing the Cs D2 line. The room temperature vapour pressure of potassium is much lower than cesium as shown in Fig. 3.3, and significant absorption is observed only when the cell is heated for the short cell length. Due to its room temperature vapour pressure, cesium is one of the commonly used alkali metals used for spectroscopy experiments, since significant absorption between 10%-50% can be observed for 5 -7 cm cell lengths at room temperature [1].

The equation for calculating the vapour pressure of potassium and cesium is taken from Ref.[14], and has the following form:

$$\mathrm{logP_v} = A - BT^{-1}. \tag{3.1}$$

Here, P_v is the vapour pressure in units of atm and T is the temperature of the atomic specimen in Kelvin. For the solid phase of cesium, the constants A and B are 4.711 log(atm) and -3999 log(atm)·K, respectively and for the liquid phase constants A and B are 4.165 log(atm) and -3830 log(atm)·K, respectively. The corresponding constants for solid potassium are 4.961 log(atm) and -4646 log(atm)·log(atm), and for the liquid phase, 4.402 log(atm) and -4453log(atm)·K. This equation is valid for temperatures between 24.85 °C and 276.85 °C for cesium and 24.85 °C and 326.85 °C for potassium. Additional

polynomial terms may be included for the vapour pressure equation, however, two terms used for this calculation suffices for a realistic vapour pressure calculation with an associated error of $\pm 5\%$ [14]. Figure 3.4 shows a plot of the calculated number densities for the same temperature range in Fig. 3.3 for cesium and potassium using the vapour pressure values from equation (3.1):

$$\mathrm{N} = \frac{101325 \times 10^{\log \mathrm{P_v}} N_A}{RT \times 10^6},$$
(3.2)

where N is the number density in units of $\mathrm{cm^{-3}}$, N_A is the Avogadro constant, R is the ideal gas constant, and T is the absolute temperature.
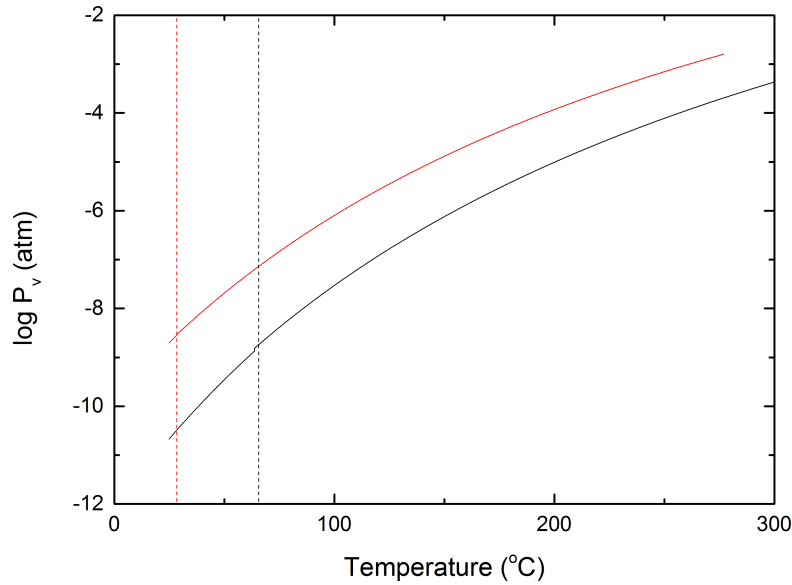
Figure 3.3: Vapour pressure of cesium and potassium as a function of temperature, plotted on a log-lin scale. The vapour pressure of cesium and potassium are indicated in red and black, respectively. The dashed line in red indicate the melting point of cesium and potassium at 28.44 °C [10] and 63.65 °C [11], respectively

To achieve higher cell temperatures, a nichrome wire is wound around the brass casing and insulated using layers of foil and insulation wool to prevent as much heat loss as possible. An air gap was created between the casing and the aluminium mount to minimise heat transfer to the optical table. Above the operating temperature limit of the transducer, the cell temperature is measured using a thermocouple.
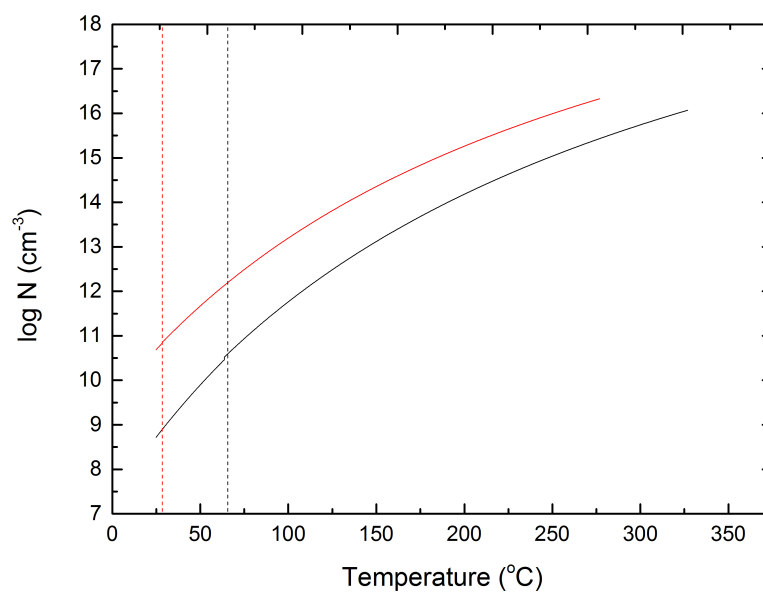
Figure 3.4: Number density of cesium and potassium as a function of temperature, plotted on a log-lin scale. The number density of cesium and potassium are indicated in red and black, respectively. The dashed lines in red indicate the melting point of cesium and potassium at 28.44 °C [10] and 63.65 °C [11], respectively.

3.2   Cesium D2 line Absorption Spectroscopy

We use a commercial diode laser supplied by Sacher Lasertechnik tuned to the Cs D2 optical transition at 852 nm. The schematic of the experimental set-up is shown in Figs. 3.5 and 3.6. The external cavity of the laser head (TEC 100) has been slightly reconfigured in the department after being repaired in the past. Output current, laser temperature and piezo voltage are controlled using the supplied laser driver (MLD 1000).
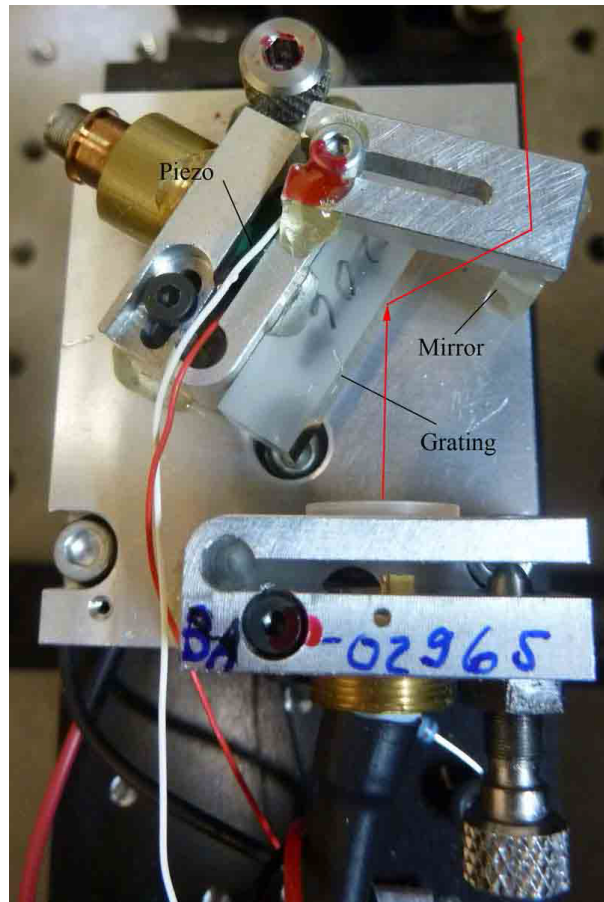
Figure 3.5: 852 nm ECDL in the Littrow configuration. The red line shows the beam path from the diode. The zeroth order beam is selected from the grating and outcoupled to the experiment using a steering mirror, and the first order beam is reflected back into the diode.

To initially set the diode current to the atomic transition, an infrared (IR) viewer is used to observe fluorescence in the cell as the optical frequency of the laser is adjusted via the current driver.

Due to changes in the operating conditions (e.g. ambient temperature), the laser was not initially scanning mode hop-free over the required range of about 9 GHz. The laser temperature was carefully adjusted in an attempt to increase its scanning range, however this resulted in the laser multi-moding. The laser was realigned using a wavemeter to the Cs D2 transition wavelength at the laser current where the transition was initially

observed, and the cavity grating realigned for a mode hop-free scan across the entire D2
spectrum. The small FSR of the laser cavity limits the mode hop free scanning range of
the laser.
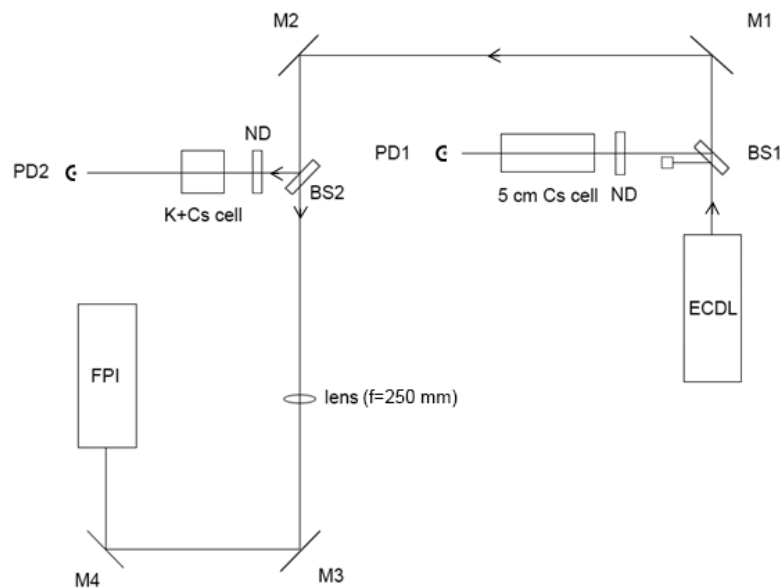
Figure 3.6: Experimental schematic for Doppler-broadened spectroscopy of Cs and K+Cs
mixture cell for the Cs D2-line. The black line leaving the external cavity diode laser (ECDL)
shows the light path for Doppler-broadened spectroscopy. The reflected light from the beam
splitter (BS1) is passed through the Cs cell and is detected by the photodiode indicated by PD1
with a $5.50 \pm 0.01 M\Omega$ resistor. The stronger light is reflected by the mirrors (M1-M4) and passes
through to a Fabry-Perot interferometer (FPI) with a free spectral range of 300 MHz to calibrate
the frequency axis. Light diffracted by the second beam-splitter (BS2) passes through a variable
neutral density (ND) filter to ensure the light entering the mixture cell is in the weak-probe
regime.

3.3 Potassium D2 line Absorption Spectroscopy

For potassium spectroscopy, a 767 nm home made ECDL is used to access the K D2 transition. A laser diode controller (Thorlabs LDC 202 C) is used to adjust the laser current and adjustment of the piezo controller (Thorlabs MDT693A) is used for small changes in the length of the external cavity in the diode laser. To scan across the transition in frequency space, a triangular waveform is fed into the piezo controller, with the amplitude of the signal leading to a proportional shift in cavity length and hence frequency. The schematic of the experimental set-up is shown in Figs. 3.7 and 3.8.
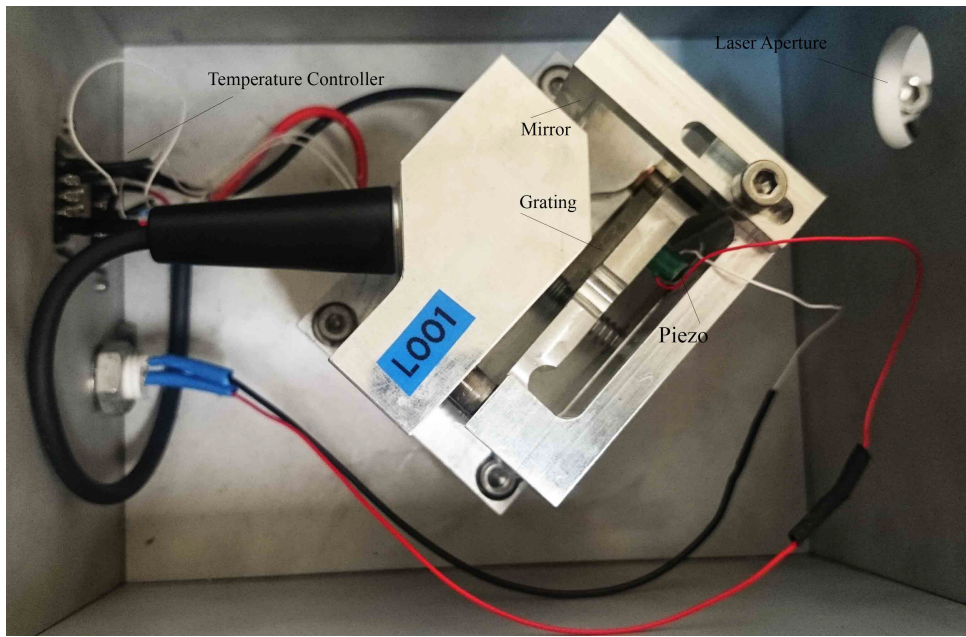
Figure 3.7: Home built 767 nm ECDL in Littrow configuration. The zeroth order beam is selected from the grating and outcoupled to the experiment.

To ensure the light entering the cell is in the weak probe regime, the probe intensity must be sufficiently weak such that $I \ll I_{\text{sat}}$, as it was detailed in section 2.1. The intensity is calculated using:

$$I = \frac{2P}{\pi w^2}, \tag{3.3}$$

where P is the measured power and w is the beam width. A variable ND filter is used to attenuate the power of the beam entering the cell. Figure 3.9 shows the transmission measured at the zero detuning of the K D2 line for the mixed cell species as a function of I/I_{sat}. The absorption quickly decreases and deviates from the predicted transmission of the weak probe regime as the probe intensity is increased, showing the importance of a weak probe intensity. The light exiting the cell is detected by photodiodes in series with a 4.40 $\pm$0.04MΩ resistance. A separate beam split off from a glass blank is used for the subtraction of the background laser power variation (laser intensity noise). A 10 cm pure
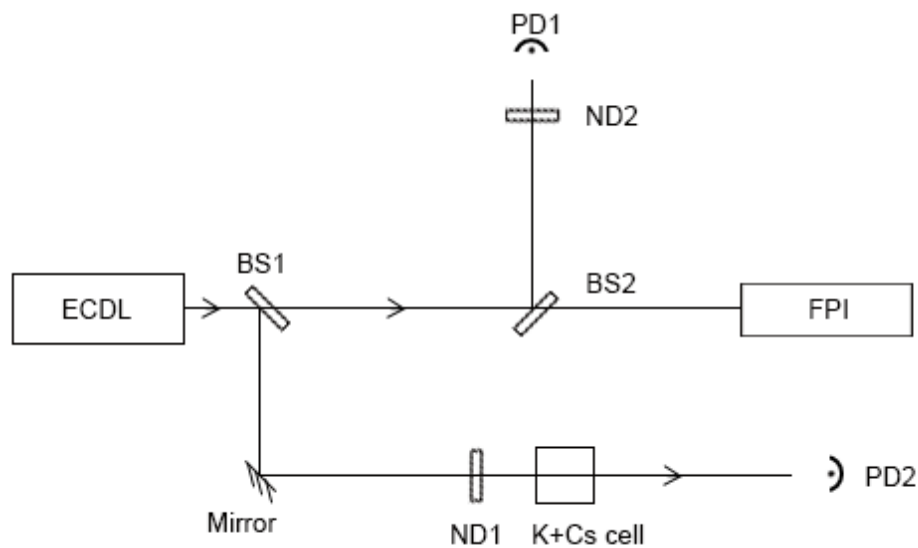
Figure 3.8: Experimental schematic for Doppler-broadened spectroscopy of K D2-line. The ND1 filter is used to ensure an even optical power into the two photodiodes (PD1 and PD2) for laser background subtraction. The ND2 filter is used to ensure the light entering the K+Cs cell is in the weak-probe regime.

potassium cell is used as a reference for finding the D2 transition as the laser is scanned across the transition, as the absorption signal is difficult to observe for up to 50 °C.
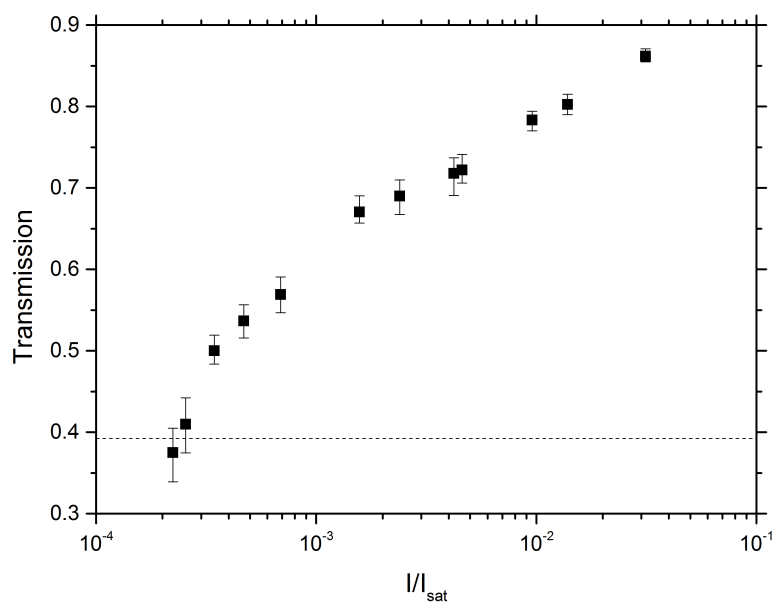
Figure 3.9: Transmission of the K D2 line measured at zero detuning as a function of I/I_{sat} for a 1 cm long K+Cs mixed species cell. The dashed line indicates the predicted transmission in the weak-probe regime, determined from measurements at the lowest probe intensities.

With the 767 nm home built ECDL, it was found that a fine scale tuning of the piezo was not sufficient to compensate for the frequency drifting of the diode laser and hence, frequent coarse adjustment of the grating angle in the cavity was necessary to tune the cavity back to resonance.

3.4 Signal Processing

To determine the transmission of the spectrum, the signal is divided by background power measued from a separate beam that does not enter the cell. An example of a raw signal is shown in Fig. 3.10. Following the division by the background power variation of the laser, the maximum transmission at a point away from the absorption features is taken to be a reference for the 100% transmission. The minimum transmission is defined as the minimum of the Dopppler-broadened absorption dip.

To calibrate the frequency axis, the signal from the FPI is used, indicated with the blue line in Fig. 3.10. The separation between the peaks of the FPI is given by the length of the cavity, and this is used to calibrate the frequency axis. The spectrum is then centered and the resulting frequency and transmission data is exported as a .csv file to upload to the Elecsus program for fitting. The processed signal is shown in Fig. 3.11.
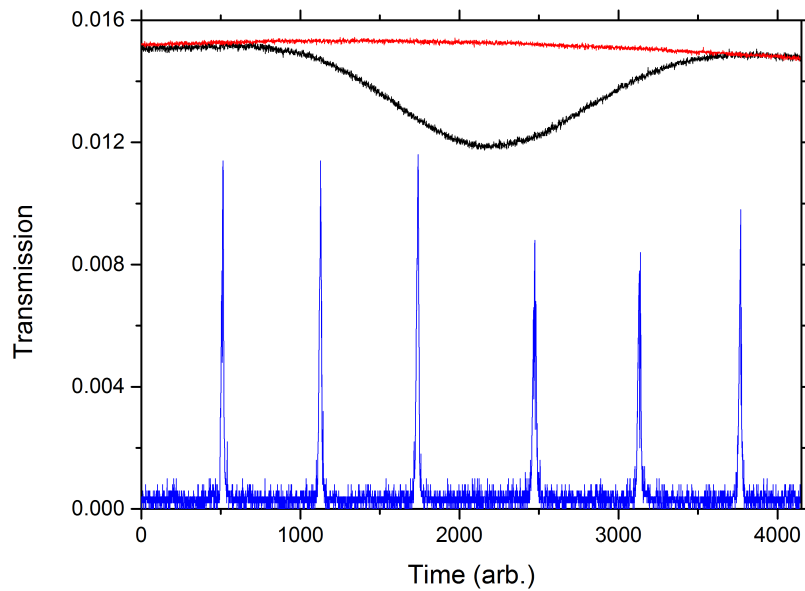
Figure 3.10: Sample of a raw signal of a Doppler broadened K D2 transmission spectrum (black) and the signal from the FPI used to calibrate the frequency scale (blue). The background laser power variation (red) is divided by the transmission spectrum, for a more accurate fitting to the experimental data.
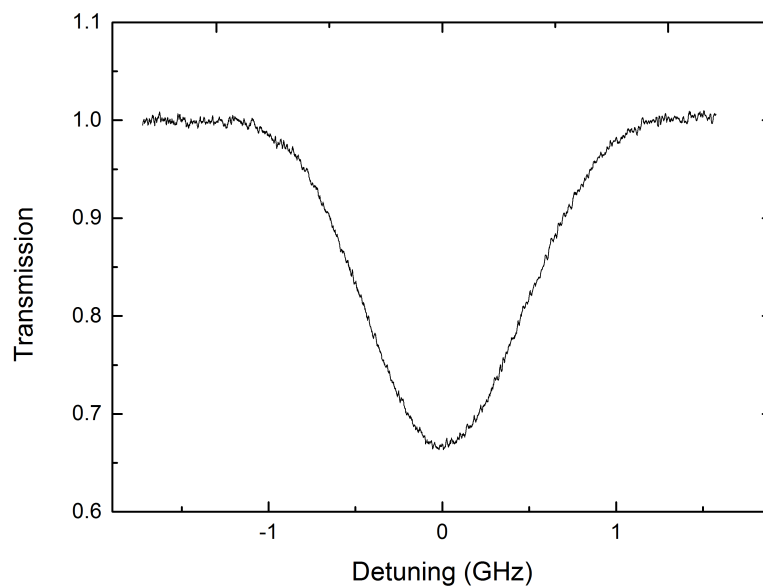
Figure 3.11: Processed signal of the spectrum in Fig. 3.10, where the maximum transmission is scaled to 1 and the frequency axis calibrated using the signal from the FPI.

3.5   Single Species Cell

The Doppler-broadened transmission spectrum of the Cs D2 line has two transmission dips corresponding to the $F = 3 \to F' = 2, 3, 4$ and $F = 4 \to F' = 3, 4, 5$ transitions of the $6^2 S_{1/2} \to 6^2 P_{3/2}$ energy levels. Figure 3.12 shows the transmission spectrum of a pure 5 cm cesium cell. All measurements are taken within the weak probe regime, with the probe beam having intensities between I=0.03-0.05I_{sat}. For potassium, I=0.004-0.007I_{sat} for all measurements.
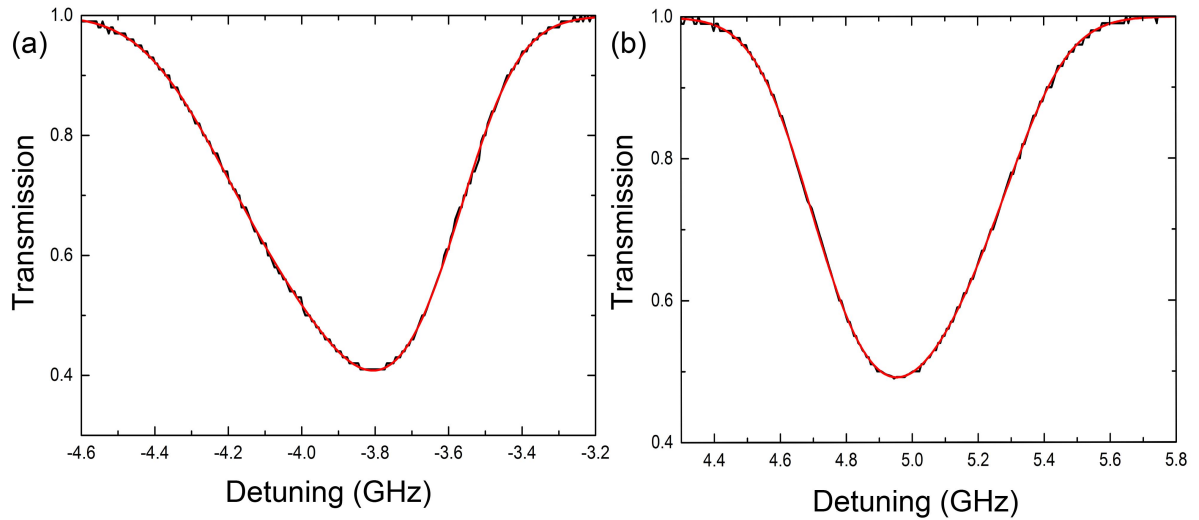
Figure 3.12: Doppler broadened transmission spectrum of the Cs D2 line for a 5 cm long, pure cesium cell, at a calculated temperature of 25°C. The black line shows the raw spectrum that has been adjacent averaged, and the red line is the temperature fit to the raw data performed by the algorithm. (a) shows the Doppler broadened spectrum for the $F = 4 \to F'$ transitions and (b) for the $F = 3 \to F'$ transitions of the $6^2 S_{1/2} \to 6^2 P_{3/2}$ energy levels

As seen in Fig. 3.12, only two transmission dips are visible. The hyperfine features are obscured due to the effect of Doppler broadening which is approximately 377 MHz at 25 °C, which is calculated using equation (2.26) using the values in Appendix A and C. This is larger than the all of the splittings in the hyperfine excited state manifold.

For the Doppler broadened spectroscopy of potassium of the mixture species cell, a 10 cm single species potassium cell is used as reference to initially find the K D2 transition. Figure 3.13 shows the transmission spectrum of this reference cell, with some hyperfine features visible due to back reflection of light entering the cell from supporting optics.
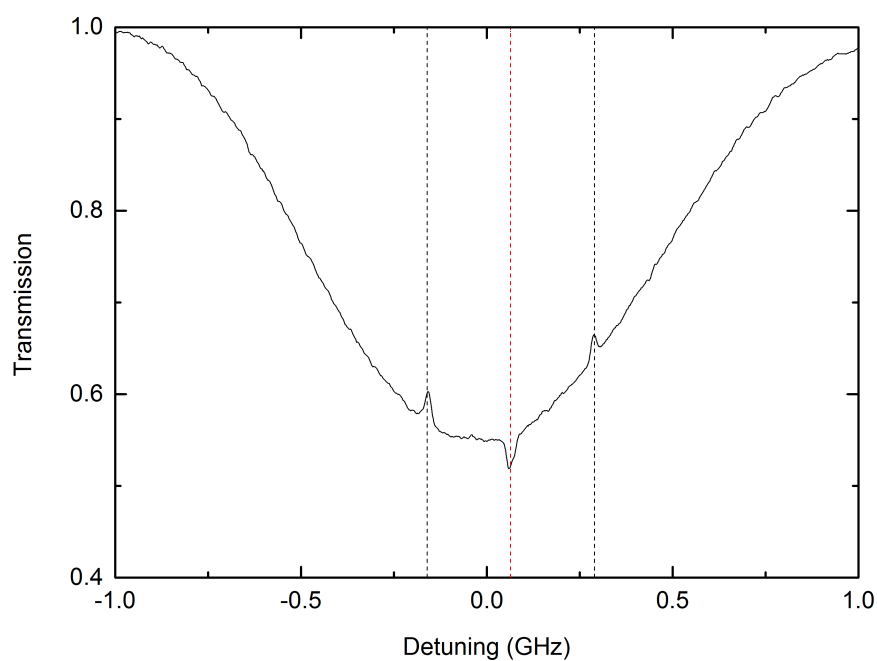
Figure 3.13: Transmission plotted against linear detuning of a pure, 10 cm potassium cell used as a reference for getting the ECDL on the K D2 transition. The approximate temperature of the cell as measured with a thermocouple is 35°C. The black dashed lines indicate the $F = 1$ and $F = 2$ hyperfine splitting and the red dashed line shows the crossover dip occuring halfway between the $F = 1$ and $F = 2$ levels.

Chapter 4

Results

4.1 Cs D2 Line

The Doppler broadened transmission spectrum of the cesium D2 lines, with the calculated transmission spectrum as a function of linear detuning are shown in Fig. 4.1. Since cesium has a sufficiently large number density at room temperature, significant absorption is observed at 24.6 °C (49% on the $F = 4$ line), and at a slightly higher temperature of 45.4 °C, there is almost complete absorption (99% absorption on the $F = 4$ line). Looking at the transmission spectrum, the centres of the transmission minima are separated by approximately 8900 MHz, which is close to the frequency difference between the $F = 3 \rightarrow F' = 4$ and $F = 4 \rightarrow F' = 5$ transitions of 8939 MHz.

The transmission for the mixed species cell for $F = 3 \rightarrow F'$ and $F = 4 \rightarrow F'$ transitions of the the $^2S_{1/2} \rightarrow ^2P_{3/2}$ states are plotted in Fig. 4.2. The solid lines show the calculated transmission for the two transitions for a pure cesium cell that is 1 cm in length. The experimental data agrees with theory, showing that the mixed species cell, using a 852 nm laser, behaves as a pure cesium cell [15].
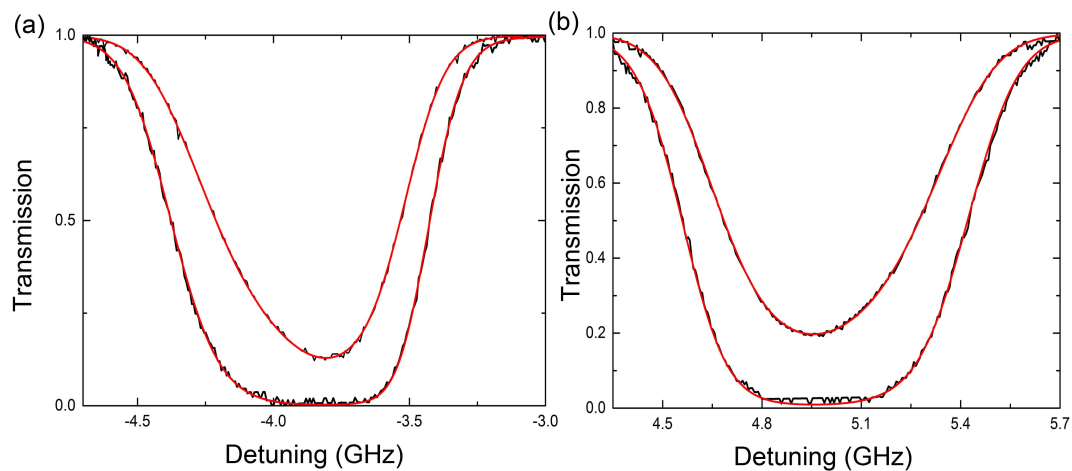
Figure 4.1: Doppler broadened transmission spectrum of the Cs D2 line for a mixed species at different temperatures. The black line shows the raw spectrum that has been smoothed, and the red line is the temperature fit to the raw data performed by the algorithm. The temperatures of the fitted curves are 24.6°C and 45.4°C for the shallower and deeper transmission spectrum, respectively. (a) and (b) show the transmission spectrum for the $F = 4$ line and $F = 3$ line, respectively.
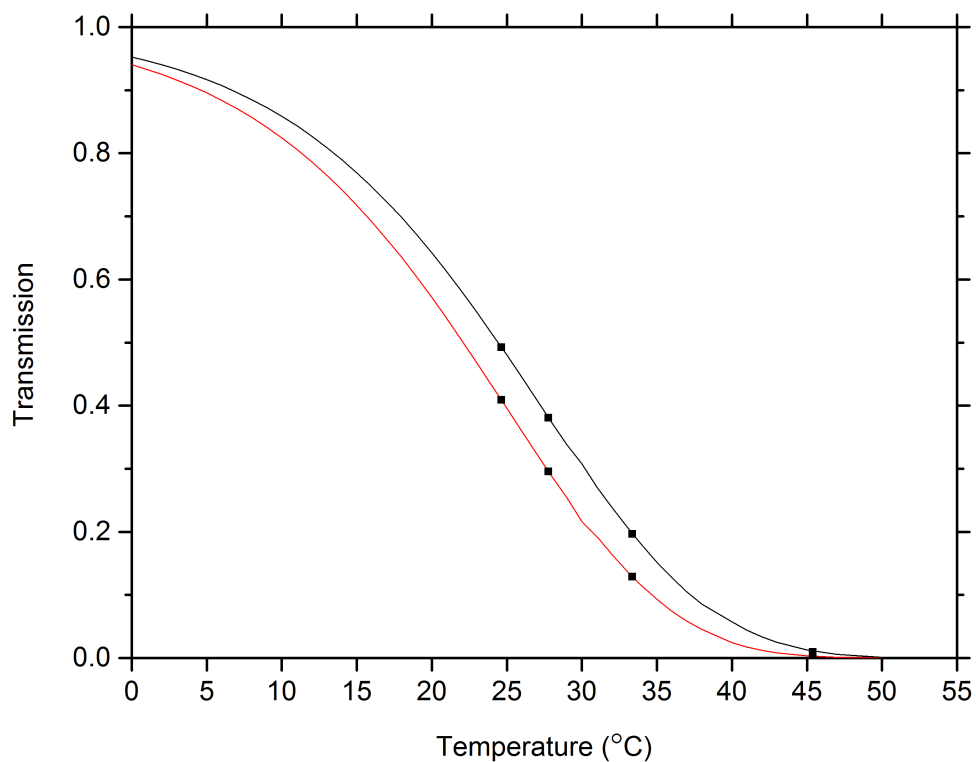
Figure 4.2: Transmission of the Doppler broadened Cs D2 line for different cell temperatures for the mixed species cell. All measurements were taken at zero detuning where maximum absorption is observed. The solid line shows the predicted transmission for a 1 cm pure cesium cell of the Doppler broadened $F = 3 \rightarrow F = 2, 3, 4$ (black) and $F = 4 \rightarrow F = 3, 4, 5$ (red) transitions.

4.2   K D2 Line

The transmission for different cell temperatures as the cell is heated is shown in Fig. 4.3. The solid line shows the predicted transmission for a pure, 1 cm potassium cell. Since cesium has a larger number density compared to potassium, the cell must be heated considerably to observe appreciable absorption on the potassium D2 line, hence the temperature range (34.8 °C - 148.2 °C) is much larger compared to the cesium plots. The transmission of the mixed species cell shows a excellent fit to the theory line, showing that the mixture cell, within this temperature range, behaves as a 1 cm pure potassium cell.
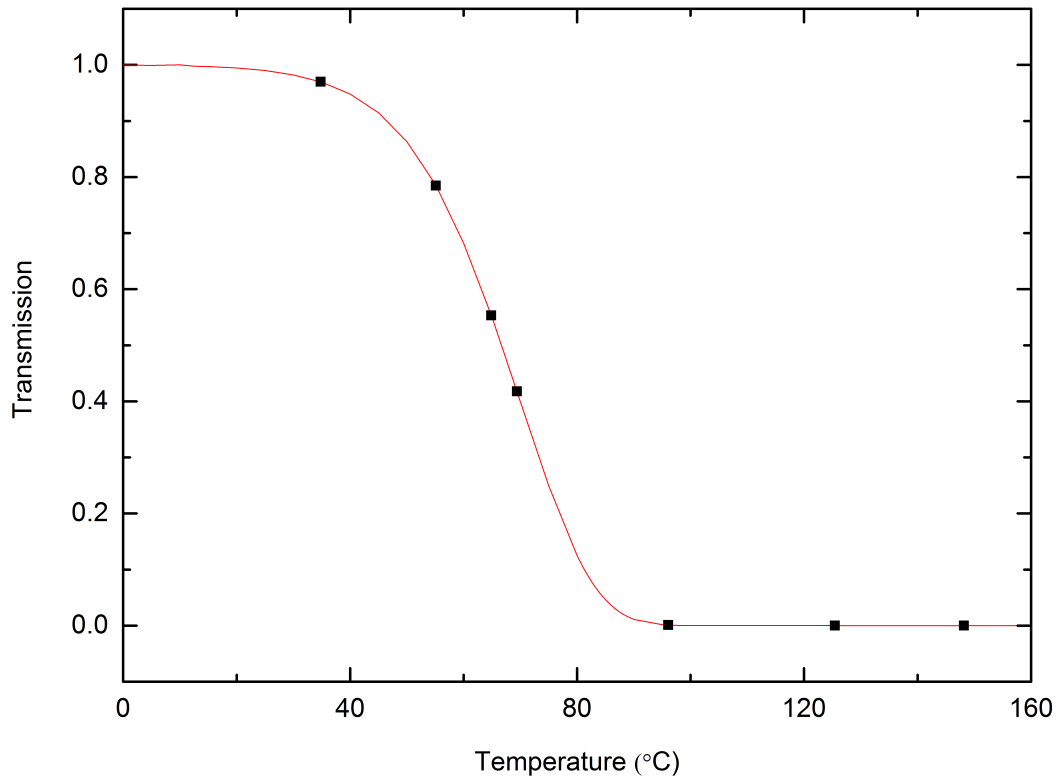
Figure 4.3: Transmission of the Doppler-broadened K D2 line at different temperatures. All measurements were taken at zero detuning where maximum absorption is observed. The solid line shows the predicted transmission for a 1 cm pure potassium cell. The temperature of the cell was measured using an AD590 transducer.

The individual transmission plots for different temperatures are shown in Fig. 4.4. Transmission is plotted against linear detuning. The red lines indicate the fit to the raw data and the theory plots at slightly different temperatures from the fit temperature are in-

cluded for comparison. The residuals indicate the degree of deviation of the experimental data from theory. In most of the transmission spectra, the agreement between experiment and theory is good, with the residuals lying within a percent deviation. In Fig. 4.4(d) where the cell temperature is 96.1 °C, the effect of off-resonant light on the maximum absorption is seen by looking at the residual plot with a 4% deviation from theory where this effect is present.

Even with the laser tuned to the transition frequency, there will be a fraction of atoms that will not be resonant with the laser due to the Doppler effect. This effectively means that the transmission dip gets bigger or smaller as a function of temperature.

Subtraction of the background laser power variation is more difficult at high temperatures. Although the background subtraction was performed to eliminate the laser intensity variation from the laser, it is clear from the asymmetrical baseline for a few of the transmission spectra in Fig. 4.4 that the laser intensity variations were not completely eliminated. This is due a combination of different factors, and includes the vapour cell windows and photodetector, or the reflecting surfaces from surrounding optics resulting in an etalon effect from amplitude modulation.

Fig. 4.5 shows a comparison of the predicted cell temperature using Elecsus and the temperature reading from the AD590 transducer. The temperature measured using the transducer consistently read a temperature higher than the calculated temperature. This can be explained by the fact that the cell was in poor thermal contact with the brass casing, resulting in a lower temperature within the cell compared to the temperature that was measured by the transducer. As seen in Fig. 3.1, the cell was loosely enclosed in the brass casing with air gaps present between the cell and the casing to prevent damage to the cell windows. This resulted in an offset temperature between the measured and actual temperature of 9 °C. Fig. 4.6 shows the relative transmissions for different cell temperatures from the fit to experimental data.

Up to a temperature of approximately 175 °C, the natural broadening is larger than the self-broadening, and for a temperature range between 175 °C and 250 °C, the contribution from the self broadened linewidth becomes greater than from the natural linewidth. For temperatures exceeding 250 °C, the Doppler width is the dominant contributor compared to the total Lorentzian linewidth. The total Lorentzian linewdth, Γ_{tot}, is defined as [1]:

$$\Gamma_{\text{tot}} = \Gamma_0 + \Gamma_{\text{self}} = \Gamma_0 + \beta N, \tag{4.1}$$

Here, Γ_{tot} is the total Lorentzian linewidth which results from the contribution of the natural linewidth Γ_0 and the self-broadened linewidth, Γ_{self}. The self broadening coefficient
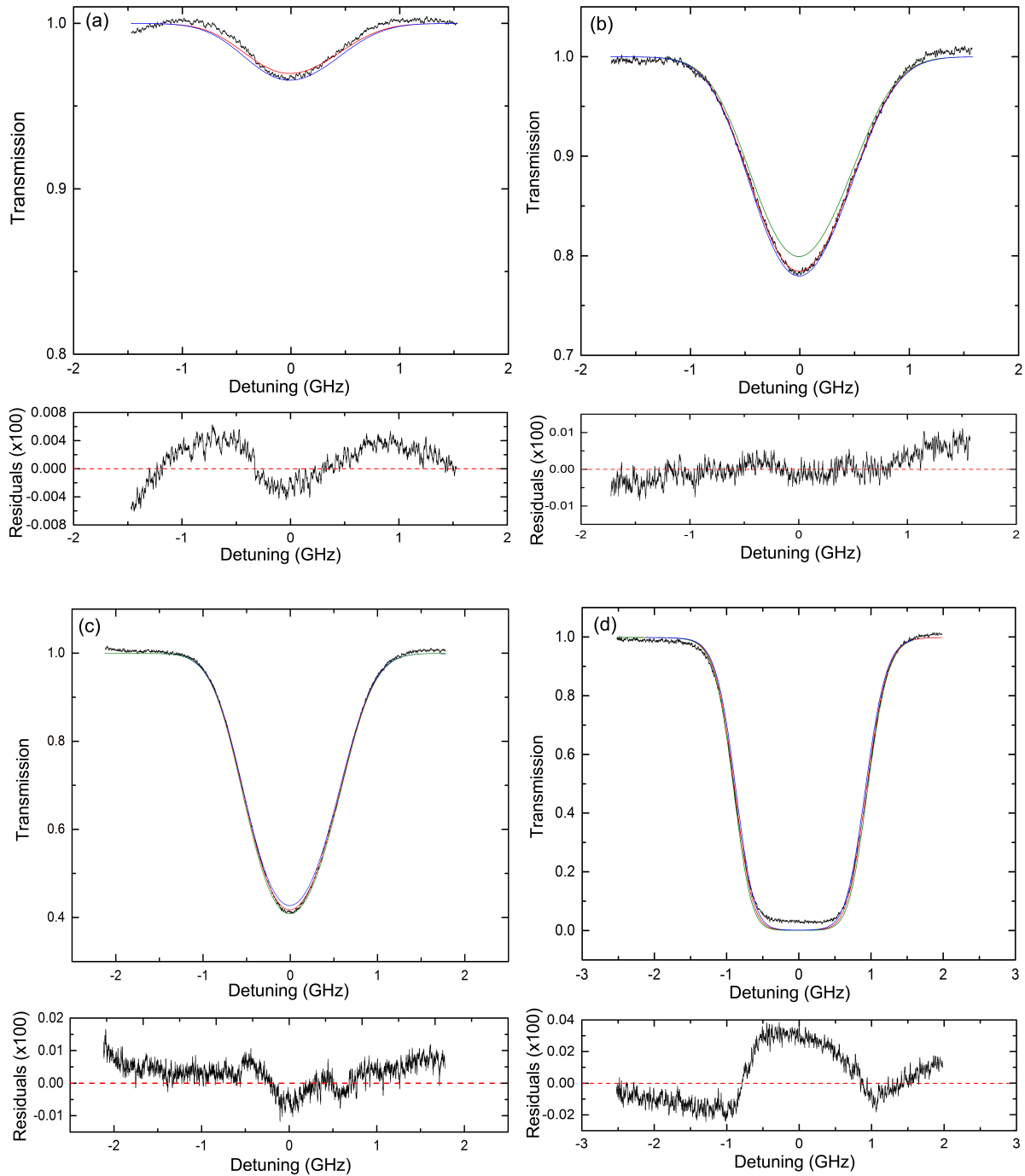
Figure 4.4: Doppler broadened transmission spectrum of the K D2 line at different temperatures. All measurements were taken at zero detuning where maximum absorption is observed. The black line shows the raw spectrum that has been smoothed, and the red line is the temperature fit to the raw data performed by the algorithm. The temperatures from the fit are (a) 34.8 °C+0.2 °C, (b) 55.1 °C+0.3/-0.8°C, (c) 69.4 °C±0.3 °C, and (d) 96.1 °C+1.0/-1.1 °C. The errors associated with the fitted temperatures are determined from the theory curves at slightly different temperatures from the fitted temperatures to illustrate the accuracy of the temperature of the fitting routine.

β for the D2 lines is defined as [1]:

$$\beta = 2\pi \times \sqrt{2}\Gamma_0 \left(\frac{\lambda}{2\pi}\right)^3. \tag{4.2}$$

For a temperature range between 34.8° C to 150° C considered in this report, the dominant broadening mechanism is Doppler broadening, which is two orders of magnitude greater than the natural broadening and between two to ten orders of magnitude greater than the self-broadening. A plot showing the different broadening mechanisms contributing to the total linewidth for the K D2 line is included in Appendix B.

From Fig. 4.6, it is clear that measurements at high cell temperatures require a larger mode hop free tuning range of the laser to resolve the full spectral range as the linewidth of the spectrum increases. The maximum mode-hop free scanning range of the ECDL after coarse adjustment of the piezo is roughly 6 GHz. This scanning range is sufficient thus far, however a larger scanning range is required to resolve the full spectral range for higher temperatures, as it is seen later. By applying a feed-forward current modulation, the scanning range is increased to 14 GHz. Hence the scanning range of the laser limits our ability to resolve the full range of the transmission spectrum.

To determine whether the presence of cesium in the cell affects the transmission spectrum of potassium, the cell temperature was further increased to induce a higher inter-atomic collision rate between the two alkali metals. At around 155 °C , we begin to observe some features on the wings of the Doppler-broadened spectrum which does not correspond to any of the hyperfine transitions of potassium, possibly indicating absorption resulting from molecular transitions. Since the transducer is not built for temperature measurements exceeding 150 °C as mentioned in section 3.1.2, a thermocouple was used for rough measurement of the cell temperature. The calculated spectrum at the measured temperatures are indicated in light green are shown in Figs. 4.7 and 4.8.

After two days of heating the cell at temperatures between 190 °C and 200 °C, the atomic mixture oxidized and acquired a yellowish tint with visible residue on the cell walls. Oxidation is a common occurrence when heating a cell to high temperatures, as observed in rubidium at high temperatures. Pyrex becomes more porous as the cell is heated to high temperatures, and as a result, the alkali metals oxidized, resulting in a weakened signal detected for both alkali metals. The accumulated residue on the sides of the cell wall is also potentially the reason for a decreased absorption signal. Possible solutions to prevent oxidation above 190 °C is to increase the glass thickness of the cell wall and to limit the measurements made to short intervals to minimize the time that the cell is exposed to high temperatures.

Figs. 4.7 and 4.8 show the transmission spectrum before the cell oxidized. A temperature
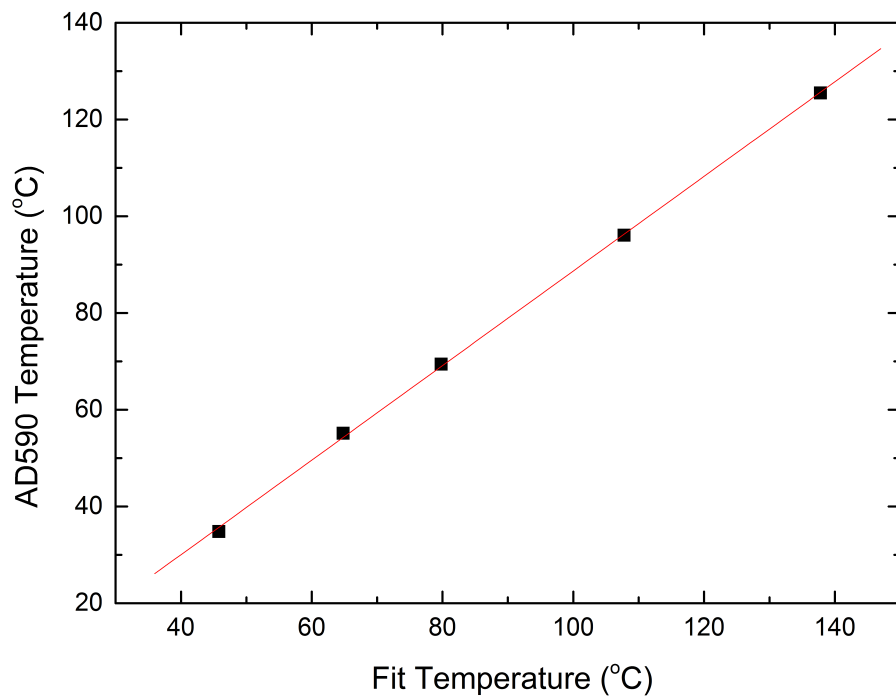
Figure 4.5: Comparison of the cell temperature measured using the AD590 transducer and the predicted cell temperature from Elecsus. The red line shows the linear fit to the raw data, where the slope from the fit is 1.0 ± 0.1 and the intercept is 9 ± 1.
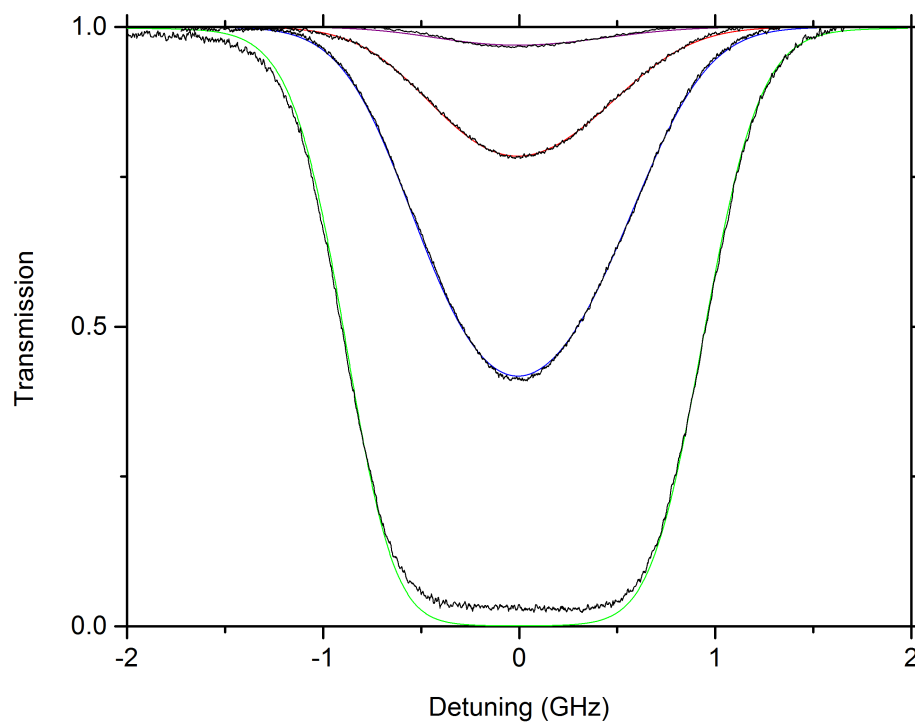
Figure 4.6: Overlay of the fitted transmission spectrum of the K D2 line for the mixture cell from Fig. 4.4. The black lines are the raw data and the temperatures resulting from the fitting routine are 32.8°C (purple), 55.1°C (red), 69.4°C (blue), and 96.1°C (green).
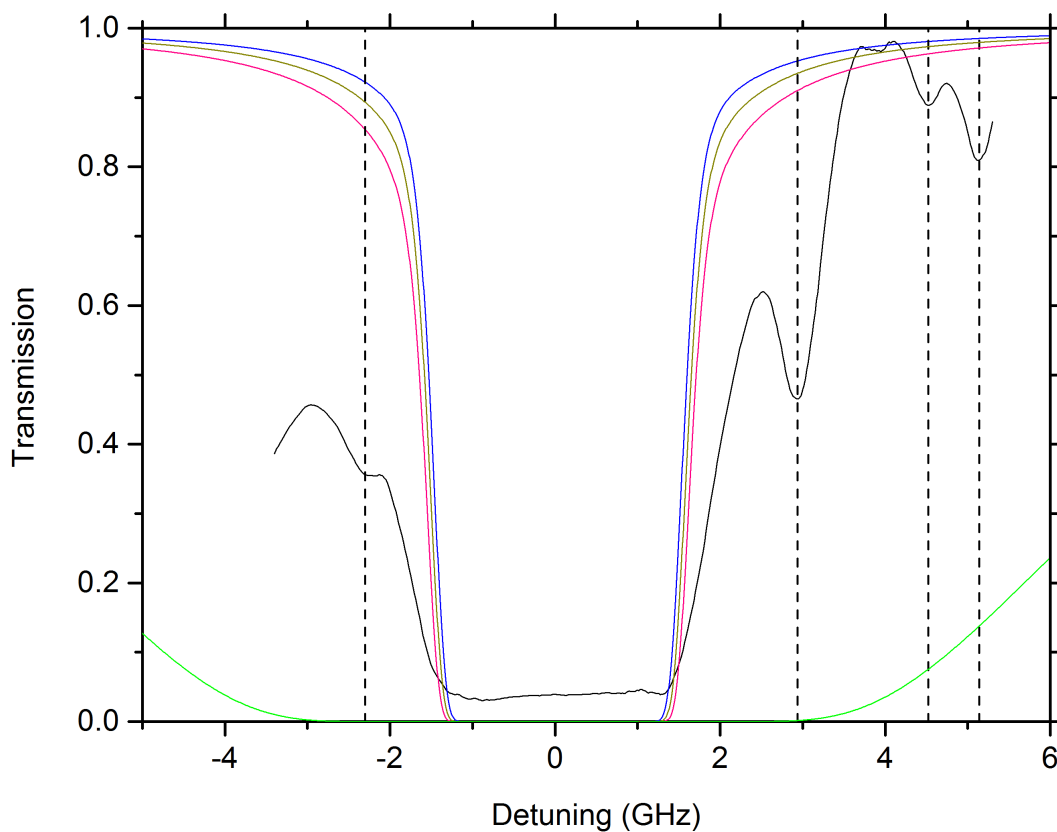
Figure 4.7: Transmission spectrum of the K D2 transition plotted against detuning at a cell temperature measured at 223 °C with a thermometer. The light green curve shows the calculated transmission profile at this temperature using a thermocouple. The cell temperature are approximated by overlaying prediction curves at 155 °C (blue), 165 °C (red), and 160 °C (dark green). The dashed lines indicate the absorption features observed at -2.3 GHz, 2.94 GHz, 4.52 GHz and 5.14 GHz.
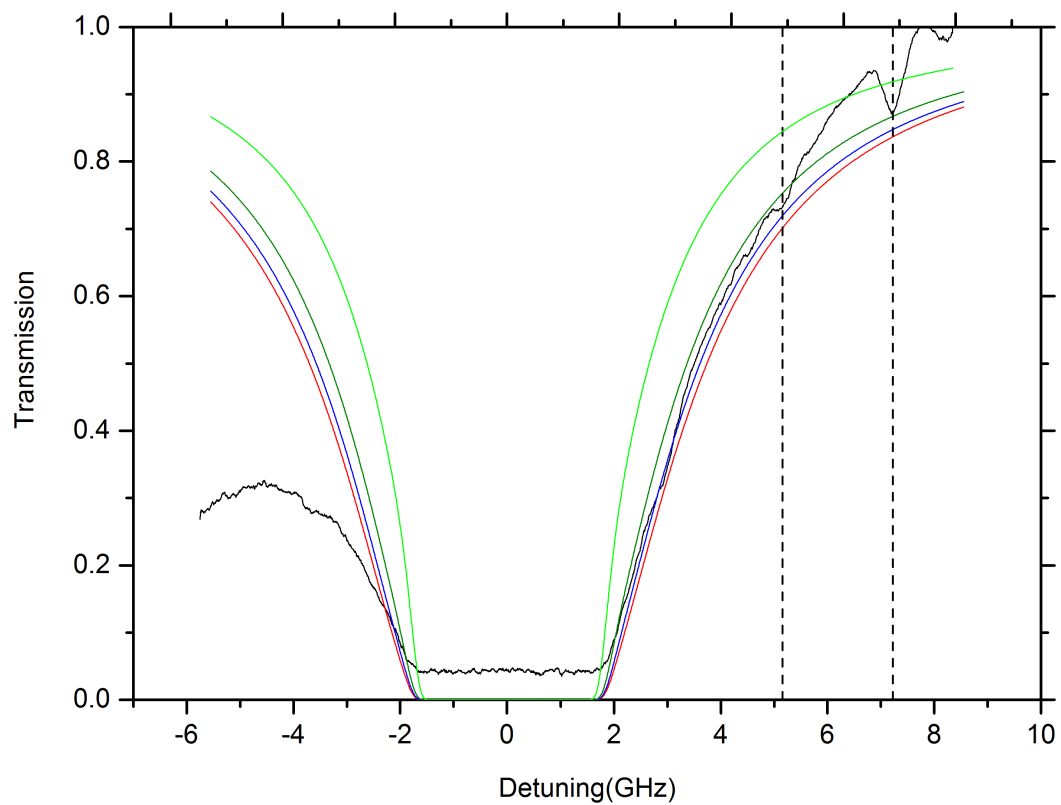
Figure 4.8: Transmission spectrum of the K D2 transition plotted against detuning at a cell temperature of approximately 199 °C, plotted with the theory curves at different temperatures. The dashed lines indicate the positions of the absorption features observed at 5.16 GHz and 7.22 GHz. The raw data measured at 190 °C is indicated in black, and the calculated spectrum at 190 °C is indicated in light green. The blue, dark green, and red curves are the theoretical spectrum at 199 °C, 197 °C, and 200 °C, respectively.

fit could not be performed on Elecsus since the background laser power variation must be subtracted, and this could not be performed since doing so results in an asymmetric baseline, as it was seen in previous results in Fig. 4.4. Predicted transmission curves are overlayed on the raw spectrum which indicate the cell temperature to be approximately 199 °C in Fig. 4.8 and 155 °C in Fig. 4.7. Since the temperature readings were made with a thermocouple, the measurements are not nearly as reliable as the transducer and as a result there is a greater discrepancy between the measured and predicted temperatures, especially in Fig. 4.7.

Fig. 4.7 was reconstructed from the bitmap image file from the oscilloscope using a program called Engauge Digitizer. We can clearly see significant absorption at 2.94 GHz from the central detuning which was not present up to 150 °C. Additional absorption features are observed at -2.3 GHz, 4.52 GHz and 5.14 GHz. This absorption observed at 5.14 GHz is also visible in Fig. 4.10 for 199 °C. Here, the larger mode-hop free scanning range shows clearly another absorption feature at 7.22 GHz from central detuning. Since these absorption features at the Doppler-broadened spectrum do not correspond to any of the K D2 transitions they are not of purely atomic nature. A potential explanation arises when the presence of $^{39}K_2$ molecules is considered. The $X_1\Sigma_g+$ ground state rotational constant of this molecule is 1.7 GHz [16]. Any electronic molecular transitions near the atomic threshold that also change rotational levels from $J' = 1 \rightarrow J = 0$ or $J' = 2 \rightarrow J = 1$ would be shifted by 3.4 or 6.8 GHz, respectively. While these values do not exactly match up with the observed dips, they indicate a possible direction for further investigation. Vibrational transitions are ruled out as they are orders of magnitude larger [17]. Further experimental work is necessary to characterise these features.

The number densities of cesium and potassium at the measured temperature of 190 °C are 1.25 $\times 10^{15}$ cm^{-3}, and 9.75 $\times 10^{13}$ cm^{-3}, respectively. Assuming the average interatomic distance is given by $\sim N^{-1/3}$, values of 9.28 μm for cesium and 21.7 μm for potassium are calculated. At the calculated temperature of 199 °C, the number densities for cesium and potassium are 1.76 $\times 10^{15}$ cm^{-3} and 1.46 $\times 10^{14}$ cm^{-3}, respectively, and the corresponding average interatomic distances are 8.28 μm and 19 μm. This shows that the number density of cesium is roughly ten times higher than that of potassium at the highest temperature that the mixture species cell was heated to.

Part II

Generating Time-Averaged Optical Potentials

Chapter 5

Introduction

5.1 Acousto-Optic Modulators

An AOM is an essential part of this trapping method as it allows for precise control of the optical dipole force generated potentials. A schematic of an AOM is shown in Fig. 5.1. The AOM is used to achieve deflection of a laser beam by a known angle with precise control. To see how this is achieved, a brief description of the AOM is given.
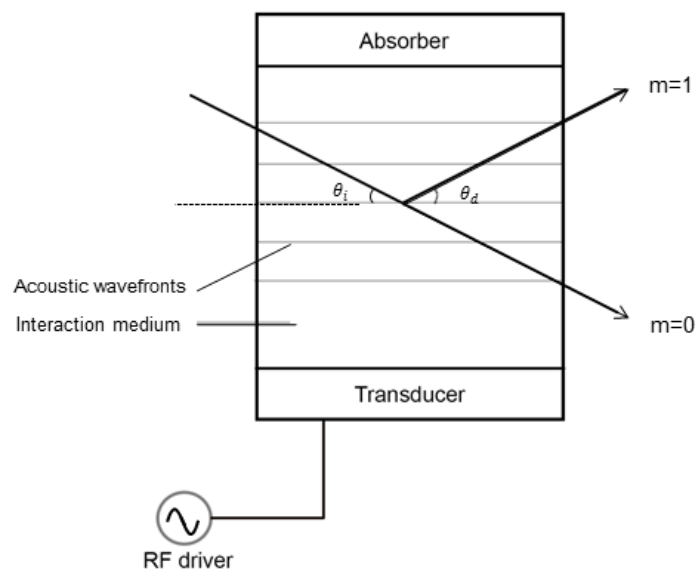
Figure 5.1: Schematic of an acousto-optic modulator. The signal from an RF driver is converted into acoustic waves which is passed into the interaction medium. The acoustic wavefronts act as gratings from which the incident laser beam with an angle θ_i is deflected into the 1st (m=1) order with an angle θ_d from the normal. m=0 corresponds to the undeflected light.

The AOM is essentially a diffraction grating created by an acoustic standing wave in an optical medium. A high frequency signal is generated from a radio frequency (RF)

driver and passes through a transducer, which converts the electrical signal to acoustic waves. The acoustic waves pass through the interaction medium, which may either be glass or crystal, creating a sinusoidal pattern from which the laser beam can diffract. If the entrance angle of the light is chosen carefully, then the AOM can deflect around 90% of the incident light into a first order beam with an angular shift given by [18]:

$$\sin(2\theta_d) = \frac{\lambda}{\Lambda_a},\tag{5.1}$$

where λ is the wavelength of the incident light and Λ_a is its wavelength. This first order diffracted beam is also shifted by the acoustic wave frequency due to the Doppler shift from the light reflecting off a moving wave front. A further benefit of the AOM is that the fraction of the initial light intensity diffracted into the first order beam is proportional to the amplitude of the driving RF wave. These characteristics essentially allow the AOM to perform the role of a beam deflector, frequency shifter and intensity modulator all in one, making it highly attractive for cold atom experiments requiring precise laser manipulation. To create a time averaged optical potential requires the rapid shifting of the position of the first order beam. This can be done very rapidly, by changing the RF frequency of the AOM driver. Typical AOMs are limited by the rise time of the acoustic wave, which is usually on the order of 10 ns [19],[20]. The rate of modulation of the laser beam also depends on the material of the interaction medium and on the beam size.

5.2   Optical Dipole Traps

Optical dipole trapping is one of the techniques of trapping neutral atoms, which relies on a weaker trapping mechanism compared to other techniques such as magnetic and radiation trapping. Trap depths of less than 1 mK are typically achieved using this method of trapping cold atoms. The main advantage of using this form of trapping lies in the diversity of geometries of the trapping potential which can be realised, such as multi-well potentials.

There are two quantities of interest when describing optical dipole potentials: the optical-dipole interaction and the scattering rate of the spontaneous emission of photons. A derivation of these quantities is outlined below, where the full derivation can be found in Refs. [21].

The goal is to describe the behavior of a free atom interacting with a laser. The laser can be considered as a classical light field $\mathbf{E}$ and the atom as a simple oscillator:

$$\mathbf{E} = \mathbf{E_0}\cos(\omega t). \tag{5.2}$$

Here, ω is the frequency of the driving field $\mathbf{E}$, and $\mathbf{E_0}$ is the amplitude of the electric field of the light. This laser will typically be far-detuned from a particular atomic resonance of the atom. The atom can be modeled classically as an electron harmonically bound to the core. This treatment remains valid, without needing a semi-classical picture, as long as saturation and consequently scattering rates remain low, which will be true for most practical dipole traps due to the large detuning. The relation between the dipole moment induced in the atom, $\mathbf{p}$, in a classical electric field of the laser is:

$$\mathbf{p} = \alpha(\omega)\mathbf{E}. \tag{5.3}$$

The complex polarizability, α is a function of the driving frequency ω, at which the atom oscillates. The interaction potential of the induced U_{dip} is obtained from the time averaged product of the dipole and the electric field vector:

$$U_{\text{dip}} = -\frac{1}{2}\langle \mathbf{p} \cdot \mathbf{E}\rangle = -\frac{1}{4}\mathrm{Re}(\alpha)E_0{}^2, \tag{5.4}$$

where the real, in-phase component of the complex polarizability, α, describing the dispersive properties of the atom is taken and the factor of $1/2$ comes from the averaging of the oscillating term. The optical dipole potential can be rewritten in terms of the intensity of the laser field as a function of position. The general expression of the laser intensity, $I = (1/2)\epsilon_0 c E_0^2$, can be substituted into equation (5.4):

$$U_{\text{dip}} = -\frac{1}{2\epsilon_0 c}I\mathrm{Re}(\alpha). \tag{5.5}$$

The optical dipole force is obtained simply by taking the negative gradient of equation (5.5):

$$\mathbf{F_{dip}}(\mathbf{r}) = \bigtriangledown\frac{1}{2\epsilon_0 c}\mathrm{Re}(\alpha)\mathrm{I}(\mathbf{r}). \tag{5.6}$$

The power that the atom absorbs from the light field is found from the imaginary component of the polarizability corresponding to dipole oscillation component that is out of phase, while substituting for intensity to get:

$$P_{\text{abs}} = \langle \dot{\mathbf{p}} \cdot \mathbf{E}\rangle = \frac{\omega}{\epsilon_0 c}\mathrm{Im}(\alpha). \tag{5.7}$$

Dividing the power by the quantised photon energy $E = \hbar\omega$ gives the scattering rate:

$$\Gamma_{\text{scatter}}(\mathbf{r}) = \frac{P_{abs}}{\hbar\omega} = \frac{1}{\hbar\epsilon_0 c}\text{Im}(\alpha)I(\mathbf{r}) \tag{5.8}$$

The simplest of the types of red-detuned dipole traps is the focused-beam trap, which is a single focused Gaussian beam. This can be used to confine atoms in a three-dimensional trap. The focused beam can be characterised by its intensity distribution and beam waist [21]:

$$I(r, z) = \frac{2P}{\pi w^2(z)} \exp\left(-2\frac{r^2}{w^2(z)}\right), \tag{5.9}$$

$$w(z) = w_0\sqrt{1 + \left(\frac{z}{z_R}\right)^2} \tag{5.10}$$

where the Gaussian beam propagates along the z axis with power P, r is the radial coordinate, $w(z)$ is the $1/e^2$ radius of the beam waist w_0 and the Rayleigh length z_R is defined as $z_R = \frac{\pi w_0^2}{\lambda}$.

To get the full expressions for the scattering rate and potential we also need the expression for the polarizability α. The derivation will be omitted but can be found in Ref. [21]. The general principle behind a classical derivation involves solving the equation of motion for a driven, harmonically trapped electron damped by dipole radiation. α can thus be expressed as:

$$\alpha(\omega) = \frac{6\pi\epsilon_0 c^3 \Gamma/\omega_0^2}{\omega_0^2 - \omega^2 - i(\omega^3/\omega_0^2)\Gamma}, \tag{5.11}$$

where ω_0 is the angular frequency of the transition between the ground and excited state of a two level atom (or alternatively the natural frequency of the classical oscillator) and Γ is the decay (damping) rate. Equation (5.11) can now be substituted into equations (5.5) and (5.8), while taking the rotating wave approximation, which ignores all terms of the form $\omega + \omega_0$ since the expressions will be dominated by $\omega - \omega_0$ terms when $\omega/\omega_0 \approx 1$ holds, which is true of most experimental conditions. The resulting potential and scattering rate for intensity given by equations (5.12) and (5.13) are:

$$\Gamma_{\text{scatter}}(\mathbf{r}) = \frac{3c^2}{\hbar\omega_0^3}\left(\frac{\Gamma}{\omega_0 - \omega}\right)^2 \frac{P}{w_0^2} \exp\left(\frac{-2\mathbf{r}^2}{w_0^2}\right) \tag{5.12}$$

$$U_{\text{dip}}(\mathbf{r}) = \frac{3c^2}{\hbar\omega_0^3}\frac{\Gamma}{\omega_0 - \omega}\frac{P}{w_0^2}\exp\left(\frac{-2\mathbf{r}^2}{w_0^2}\right). \tag{5.13}$$

5.3 Spatial Light Modulators: An Alternative to AOMs

An alternative method of generating arbitrary trapping potentials is to use a spatial light modulator (SLM) to implement phase patterns which are calculated using an iterative Fourier Transform algorithm (IFTA). The calculated phase is implemented with the SLM, and the intensity measured in the image plane. SLMs consist of a liquid crystal (LC) array, which are addressed individually by a computer, and are categorized into two types: nematic and ferroelectric SLMs. The main disadvantages of using an SLM lies in the slow update frequency (switching rate). Ferroelectric SLMs have switching frequencies a 1 kHz, whereas the nematic type SLM have switching frequencies on the order of a 100 Hz [22]. This faster update rate comes at a cost of a limitation in the range of arbitrary potentials it can generate, since ferroelectric SLMs can only take binary values. In comparison, AOMs have a switching rate on the order of 10 MHz, allowing smooth arbitrary potentials to be generated.

Another advantage of using an AOM for providing potential traps for ultracold atoms is that the trapping region is not restricted to the image plane, unlike the SLM. Another limitation is the noise which is present in the trapping plane, which can perturb the trapped atoms in the system.

The performance of the trapping potentials are characterised by its smoothness and efficiency. A smooth potential is essential to prevent heating of BECs, and a high optical efficiency is necessary for minimal loss of light to different diffraction orders. With the SLM, there is an additional need to accurately reproduce the original target pattern by empirically optimising the phase. Even with a good starting phase, the imaged trap usually requires further feedback process before implementation to the experiment [23].

A combination of both the AOM and SLM have been demonstrated to manipulate cold atoms in multiple red-detuned traps and addressing individual lattice sites [5].

Chapter 6

Simulation of Time-Averaged Potentials

There are various methods to generate potentials for trapping cold atoms using an AOM. One of the methods involve the superposition of static frequencies to create a flat box potential for atomic condensates and can be also be extended to create other continuous trapping geometries [22]. Further feedback processes can be used for optimising the trapping potential.

An alternate method involves a rapid deflection of a single Gaussian beam to create a time-averaged potential. Atoms have successfully been confined in such potentials in a red-detuned potential with minimal heating of the trapped atoms [22]. By dithering a single beam, it is possible to achieve a trapping potential with a flat region where atomic condensates can ultimately be trapped. Flat potentials are of interest in trapping BECs in optical lattices. Superimposing these flat potentials with an optical lattice of BECs, this provides a way of simulating electrons in solid-state systems in a closer way than is done in current optical lattice experiments.

Rapid deflection of a single Gaussian beam creates a time-averaged potential which can be modeled as the superposition of multiple Gaussian beams. This effect is simulated for a one dimensional trap using a MATLAB program, and is illustrated in Fig. 6.1. For a one dimensional trap, the intensity distribution given in equation (5.9) reduces to:

$$I(r, z = 0) = \frac{2P}{\pi w_0{}^2} \exp\left(-2\frac{r^2}{w_0{}^2}\right) \tag{6.1}$$

for a single Gaussian beam. The intensity of the summed trapping potential I_{tot} can be expressed as:

$$I_{\text{tot}} = \frac{2P}{\pi w_0{}^2} \frac{1}{N} \sum_{i=1}^{N} \exp\left(-2\frac{(r-r_i)^2}{w_0{}^2}\right). \tag{6.2}$$

The full expression for the summed optical dipole potential is then given by:

$$U_{\text{dip}}(r) = \frac{3c^2}{\hbar\omega_0^3} \frac{\Gamma}{\omega_0 - \omega} \frac{P}{w_0^2} \sum_{i=1}^{N} \exp\left(\frac{-2(r-r_i)^2}{w_0{}^2}\right), \tag{6.3}$$

where r is the variable position coordinate and r_i is the position of the ith Gaussian. The total intensity and hence the trapping potential is given by summing over all of the Gaussians.

As the number of superimposed Gaussians is increased, the resulting potential is smoother. For trapping atomic condensates, a smooth potential is desirable for minimising heating of the trapped particles [2]. The overall trapping potentials, shown in red in Fig. 6.1 consists of different numbers of Gaussians, shown in blue, with s denoting the step size which is the distance between two consecutive Gaussians. The dither range, denoted with an "A" is defined as the distance between the constituent Gaussians at the minimum and maximum positions.

The code has various adjustable constants and those used throughout this report are listed in Appendices C.1 and C.2. The trapping potentials are calculated for the D2 transition of rubidium 85, but the resulting difference in the calculated potential for rubidium 87, which is the other commonly used isotope in BEC experiments, is very small, and the constants can be adjusted for the specific needs of the experiment.

The aim is to achieve a trapping potential with the highest resolution possible. In theory, the highest possible resolution of a trapping potential consists of an inifinite number of Gaussians. To simulate this best case potential without compromising the run time, we look at the percent change in the trap depth by increasing the number of the constituent Gaussians. When the percent difference becomes negligible on the order of a thousandth of a percent, the number of Gaussians used to generate this potential is considered the "best case" potential. Using this best case potential, the Root-Mean-Square (RMS) deviation of the dither beam potential of linearly spaced Gaussians is calculated for different step sizes in order to determine the step size needed to simulate a potential that is effectively the same as this best case potential. The RMS error will henceforth be just referred to as RMS.

There are two free parameters in generating a dithered potential: the number of Gaussians and the dithering range. We can consider two separate cases where we vary one of the parameters and keep the other fixed. The first involves calculating the RMS of a fixed

(a)

(b)

(c)
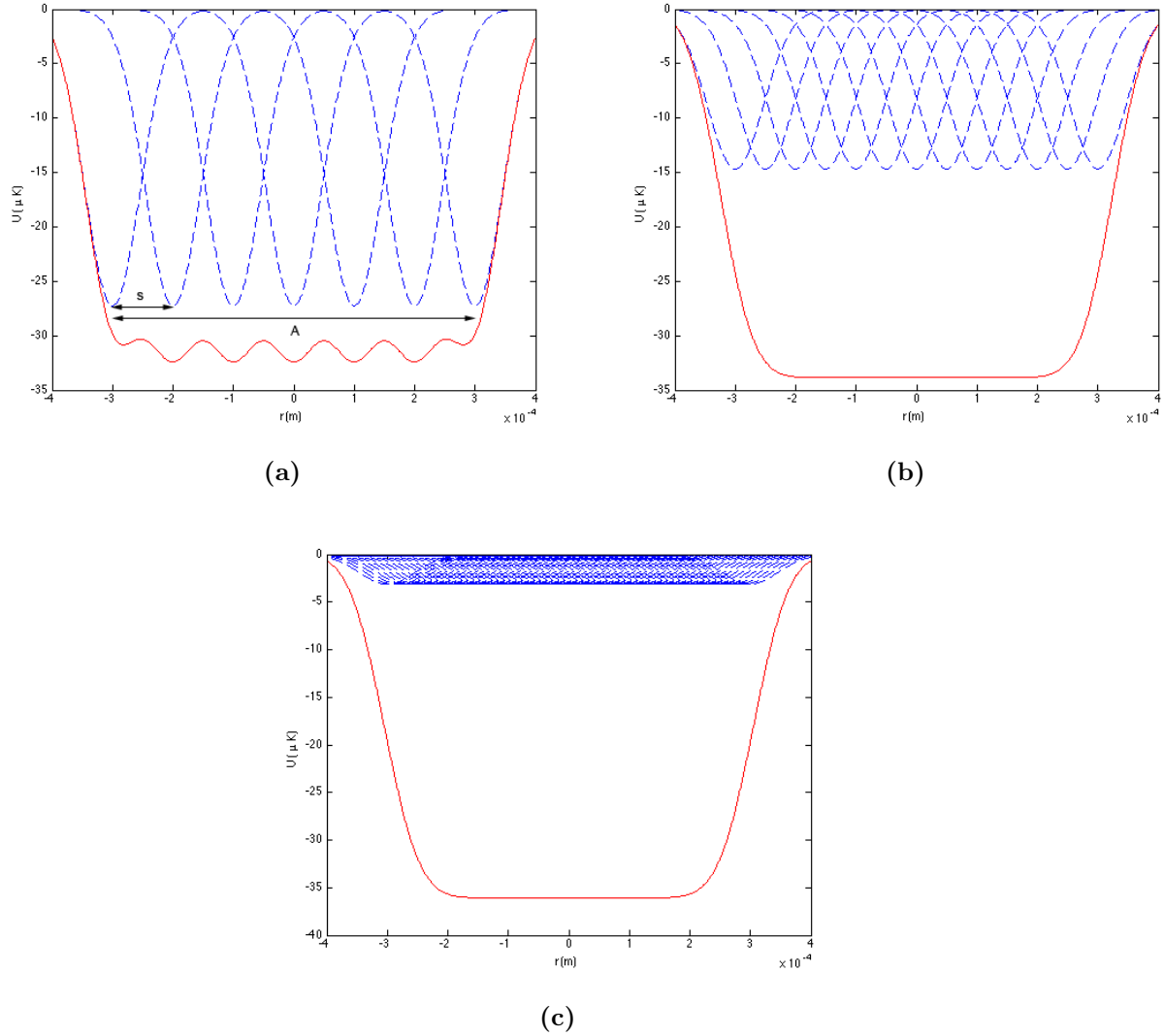
Figure 6.1: (a)-(c) shows the process of simulating a dithered Gaussian beam by superimposing multiple Gaussians, where adding a larger number of Gaussians result in a smoother summed potential. The summed potential is shown in red and the constituent Gaussians are shown in blue for (a) 7 constituent Gaussians, (b) 13 Gaussians and (c) 61 Gaussians. In the code, the summed potentials are normalised by dividing the calculated intensity by the number of Gaussians.

dither potential with a variable number of Gaussians compared to a best case potential. We present a similar case where the dither range is set as a fixed parameter while the number of Gaussians is a free parameter using dimensionless units. This is accomplished by making the units of the beam waist of the moving beam dimensionless and setting the dither range to be a power sequence of base 2 so that the total number of Gaussians is chosen such that they are evenly distributed about a central point. By using dimensionless units, the relationship between the two parameters can be easily seen.

In the second case, the dither range is set as a free parameter while the number of Gaussians used to generate the dithered potentials remain constant. An example of the code for characterising the RMS using the first method is listed in Appendix D.

6.1   Fixed Dither Range

For n number of Gaussians, the step size gets smaller by a factor of $1/n$. Since we proceed by adding one Gaussian at a time, the curve resembles a harmonic sequence in step size. The code works for any dither range by always centering the Gaussian intensity pattern, while ensuring that it remains symmetric. This is achieved by small shifts in the minimum or maximum dither point. This will introduce a small difference between the input dither range and the effective dither range used in the code. By programming it in this way, there are no restrictions on the step sizes of the dithered potential. The best case trapping potential consists of 1001 Gaussians, since the difference in RMS between using 1001 Gaussians and the next order of magnitude is on the order of a thousandth of a percent. The specific number was chosen to be within the highest possible precision, while maintaining a manageable run time.

The trapping potentials for select number of Gaussians are shown in Fig. 6.2. The RMS is calculated over the entire trap depth and the truncated region, which corresponds to a tenth of the total trap depth where BECs are confined. From the RMS calculation over the truncated region in Fig. 6.3, s/w_0 should be at least 0.83 for a trapping potential which has an RMS deviation of less than a percent from the best case potential having a s/w_0 value of 0.005. The corresponding plots of residuals are shown in Fig. 6.4.

(a)

(b)
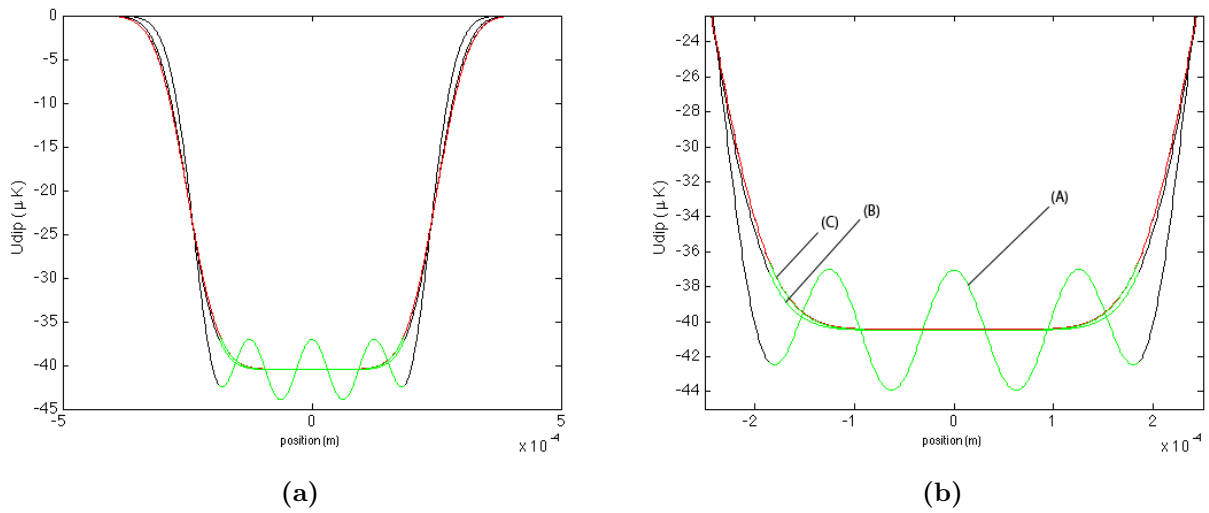
Figure 6.2: (a) Plot of dithered trapping potentials (black), best case potential containing 1001 Gaussians (red), and a tenth of the total trap depth of the dithered trapping potentials over which the RMS is calculated (green). (b) shows the same plot as (a) but over a smaller distance to distinguish the trapping potentials for different dither ranges. Labels (A)-(C) corresponds to dithered potentials with a s/w_0 value of (A) 1.25, (B) 0.625, and (C) 0.1.
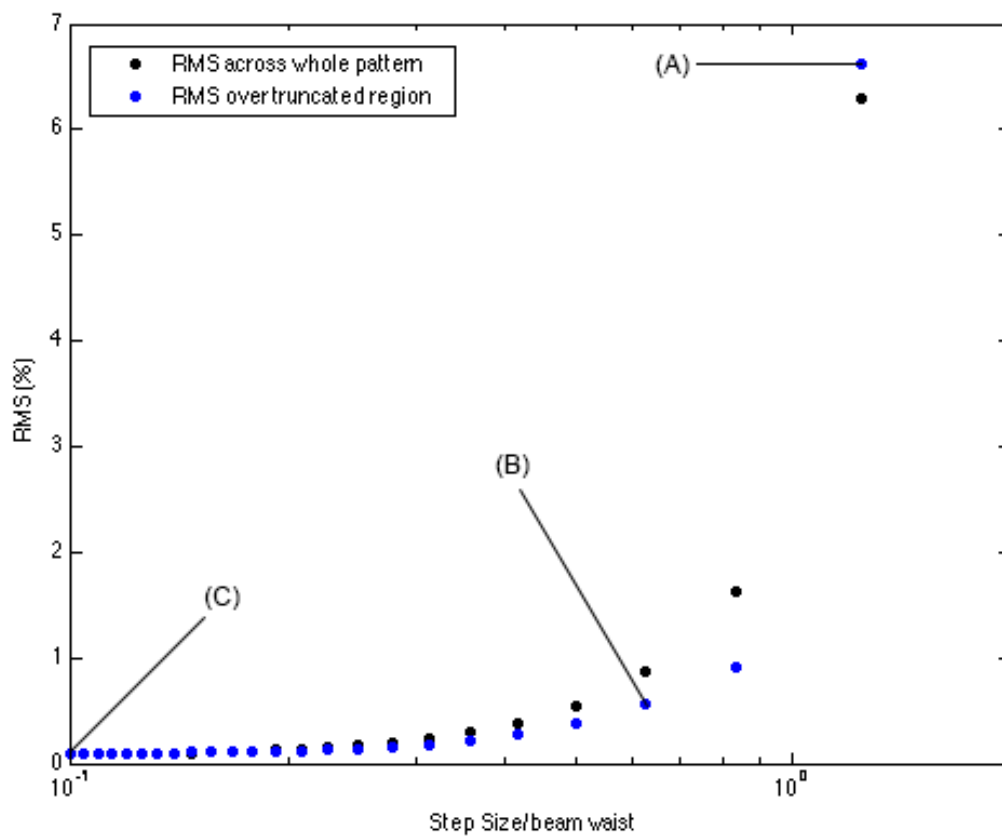
Figure 6.3: RMS across the entire pattern (black) and the truncated region corresponding to a tenth of the total trap depth (blue) of a dithered potential with the Gaussian number set as a free parameter between four Gaussians and 50 Gaussians in steps of two Gaussians, on a semi-logarithmic scale. Labels (A)-(C) corresponds to dithered potentials with a s/w_0 of (A) 1.25, (B) 0.625, and (C) 0.1, and also corresponds to the potential plots labeled in Fig. 6.2 (b)

(a)

(b)

(c)
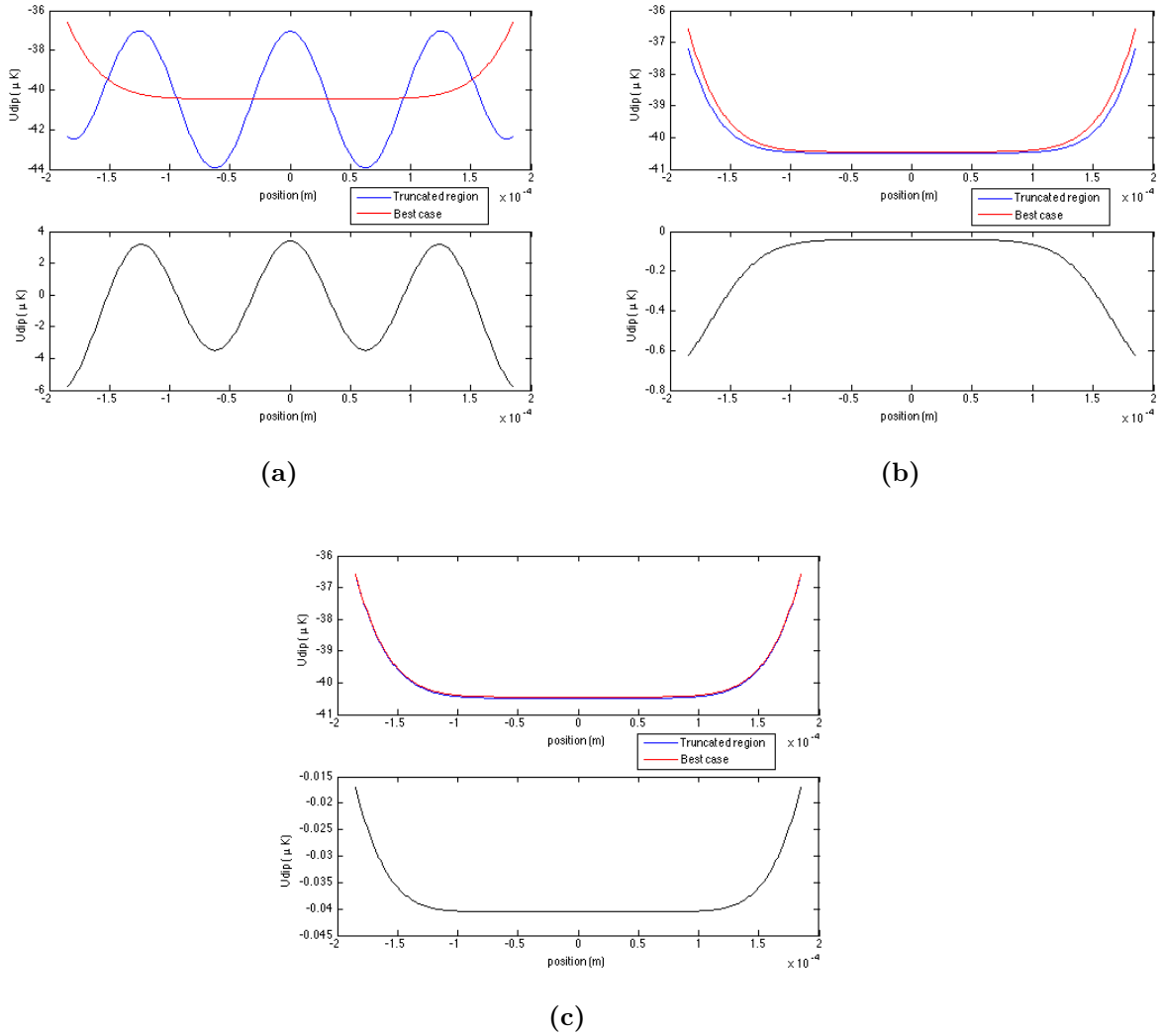
Figure 6.4: The top subplots (a)-(c) show the trapping potential of the truncated region (blue) and the best case potential having 1001 Gaussians (red). The bottom subplots show the residuals for each corresponding dither ranges having a s/w_0 value of (a) 1.25, (b) 0.63, and (c) 0.10. Note: (a)-(c) correspond to labels (A)-(C) in Figs. 6.2 and 6.3.

6.2   Fixed Dither Range in Dimensionless Units

An alternative method of calculating the RMS for a fixed dither range is to set the dither range to be $2^{n_{max}}$, and increment the dither range in steps of 2^n where n can take integer values of $n = 1, 2, 3, ...n_{max}$. This method allows the position coordinate to be dimensionless. A single Gaussian is added at each point 2^n from the origin, giving a total of $\frac{2^{n_{max}}}{2^n} + 1$ Gaussians for a dithered trapping potential. In this method, the case for which $n = n_{max}$ is excluded since this trapping potential will consist of two Gaussians placed at the origin and $2^{n_{max}}$ and does not represent a realistic dithered potential in an experimental setting. The trapping potential plots for select Gaussian numbers are shown in Fig. 6.5. Although the all of the trapping potentials in Fig. 6.5 have the same dither range, the trapping potential consisting of three Gaussians shown in Fig. 6.5 (A) appears wider than (B) or (C) because there is minimal overlap between the Gaussians. Adding more Gaussians results in a greater overlap of Gaussians and the resulting appearance of the trapping potential is narrower, as seen in Fig. 6.5 (B) and (C).

The code requires the Gaussian beam waist to be set to approximately 25% of the maximum dither range for a realistic beam waist compared to the dither range. The best case trapping potential is set to have unit step size, and the dithered potentials for a particular value of n_{max} have $2^{1,2,...n_{max}}$ step sizes. For a dither range with $n_{max} = 12$, the RMS across the entire pattern and over the truncated region of a tenth of the total trap depth drops below a percent deviation from the best case potential if there are 129 and 65 Gaussians in a dithered potential, respectively. This threshold occurs at a s/w_0 value of 0.0059 and 0.0049, respectively. The RMS plots are shown in Fig. 6.6, and the corresponding residuals are shown in Fig. 6.7.
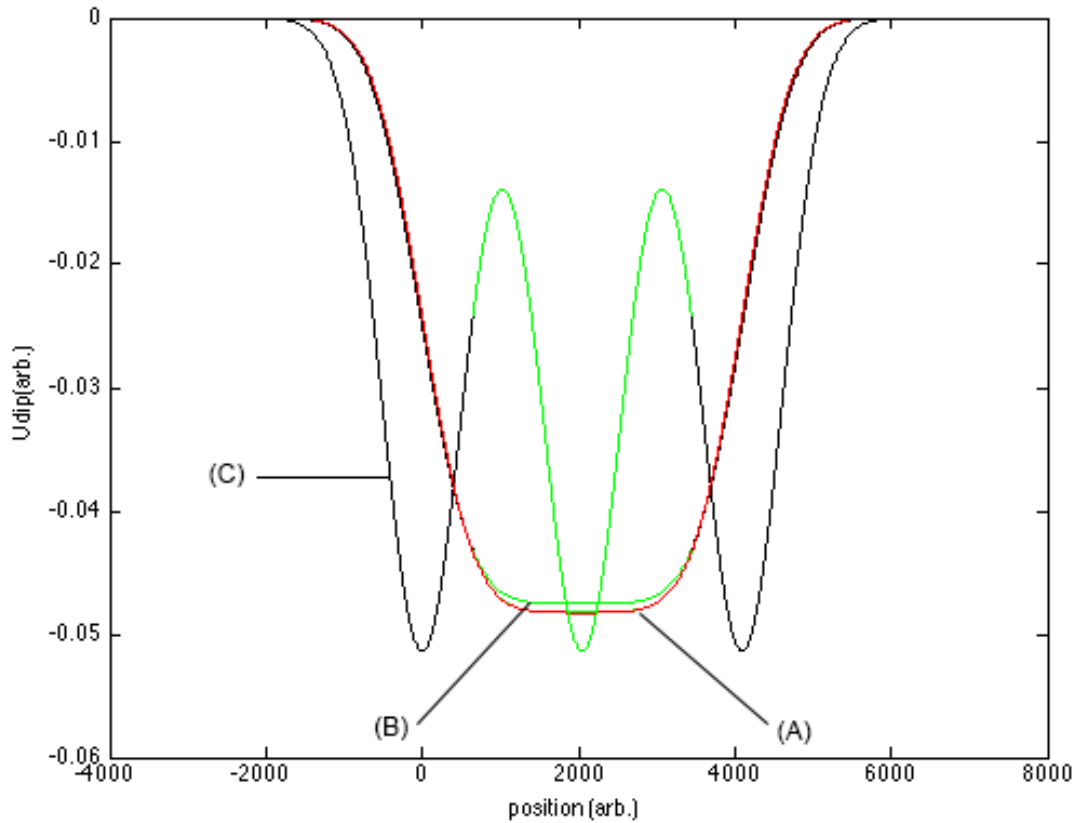
Figure 6.5: Dithered trapping potentials for a dither range of $2^{n_{max}}$ where $n_{max} = 12$. The best case potential is shown in red and has a total of $2^{n_{max}}$ steps, or 4096, corresponding to (A) in Fig. 6.7 . The trapping potentials with different Gaussian numbers are shown in black and the green indicates the truncated region corresponding to a tenth of the total trap depth over which the RMS deviation from the best case is calculated. The dithered potentials have 2^n step sizes where n = $1...n_{max}$. For a dithered potential with 2^n step size, the number of Gaussians is equal to $\frac{2^{n_{max}}}{2^n} + 1$. There are 2049, 65, and 3 constituent Gaussians for plots (A)-(C), respectively. The beam waist is set to be 25% of the total dither length, or 1024.
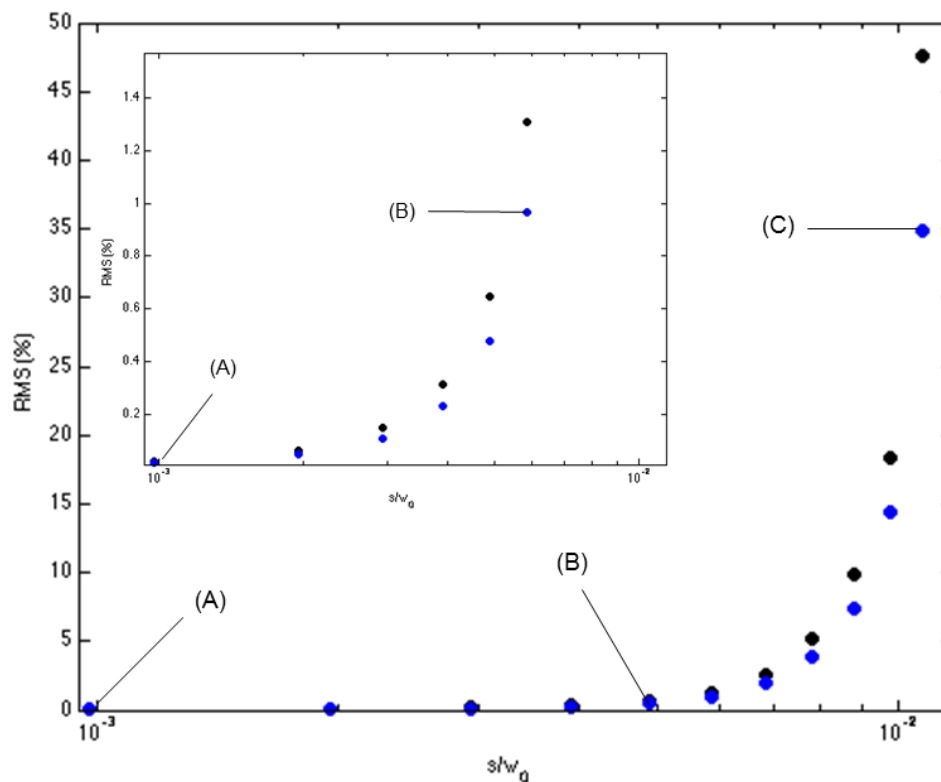
Figure 6.6: RMS calculation across the entire trapping potential (blue) and over the truncated region (black). The RMS lies within a percent deviation from the best case potential across the entire pattern and over a tenth of the total trap depth for a s/w_0 value of at least 0.0059 and 0.0049, respectively. The inset shows the plot on a smaller scale to highlight the smaller RMS deviation between points (A) and (B).

(a)

(b)

(c)
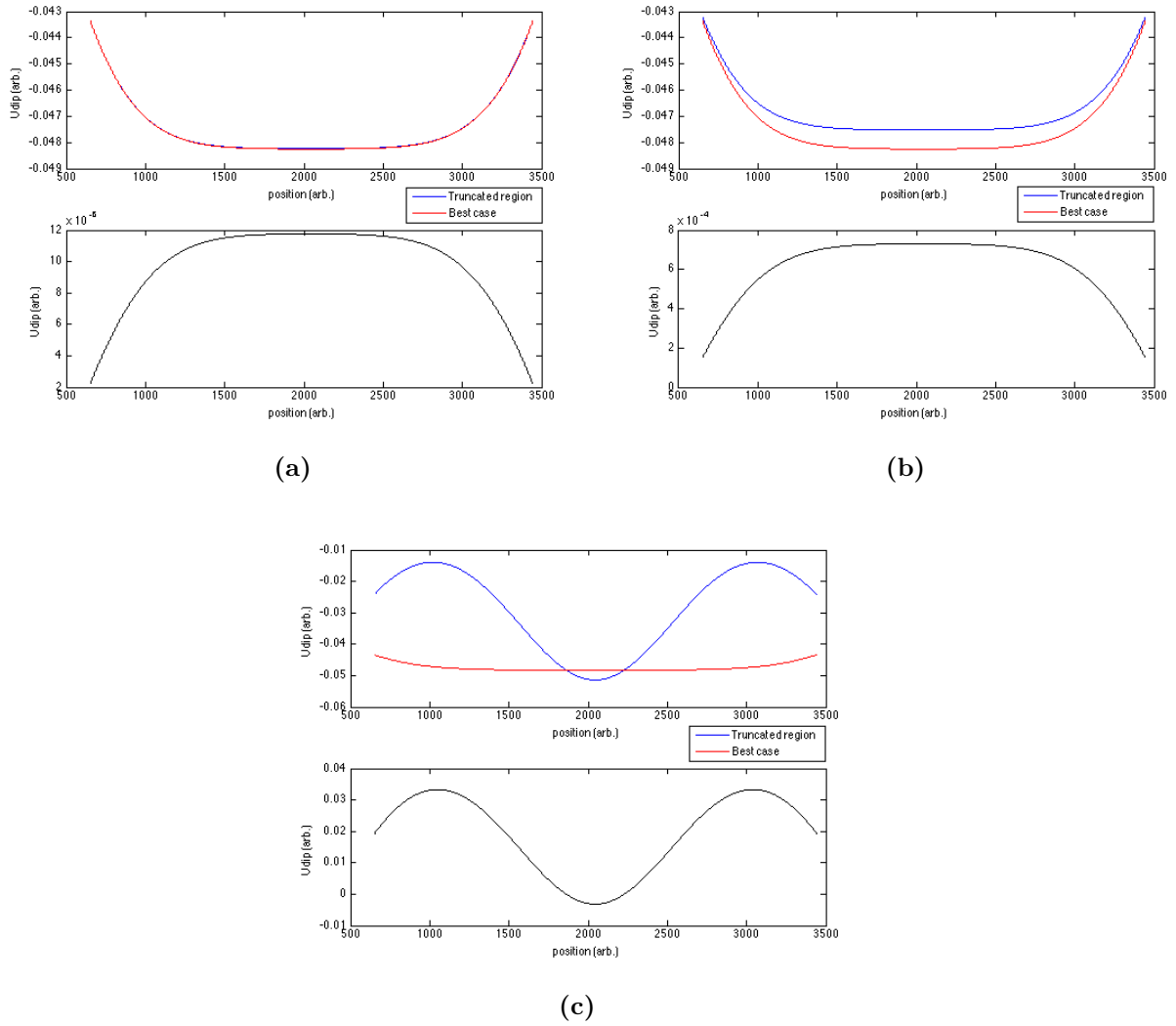
Figure 6.7: The top subplot of (a)-(c) show the trapping potential of the truncated region (blue) and the best case potential having 1001 Gaussians (red). The bottom subplot show the residuals for each corresponding to labels (A)-(C) in Fig. 6.5. The s/w_0 value of (a)-(c) are 9.77×10^{-4} (2049 Gaussians), 59.00×10^{-4} (65 Gaussians), 107.00×10^{-4} (3 Gaussians), respectively. The RMS values over the truncated region for (a)-(c) are 0.02%, 1.31%, and 47.55%, respectively.

6.3 Free Dither Range

For the case where the dither range is set as a free parameter, it is possible to calculate the RMS of as many step sizes as desired since for a specified number of Gaussians, the code ensures a symmetric distribution of Gaussians for a particular dither range. The trapping potential plots for select dither ranges are shown in Fig. 6.8 and the RMS calculations are shown in Fig. 6.9. In the previous case, the dither range is set as a fixed parameter and the dithered potentials with different Gaussian numbers are compared against the same best case trapping potential. However, for the case where the dither range is varied, each dithered potential has the same Gaussian number but different dither ranges. To calculate the RMS error associated with each dithered potential, the dithered potentials with a particular dither range are compared against a best case potential with the same dither range but with the number of Gaussians set to be 100 times greater than than that used to generate the dithered potentials. This potential with a larger number of Gaussians is considered the "best case" potential, which is used to calculate the RMS error across the entire pattern and across the truncated region.

The Gaussian number used to generate the best case potential is chosen so that the RMS saturates for a particular number of Gaussians used to generate the trapping potentials with varying dither ranges. For the case where 12 Gaussians are used to generate the trapping potentials, the best case potential consists of 1101 Gaussians since increasing this number to the next order of magnitude results in an RMS change on the order of a thousandth of a percent. The potential plots for select dither ranges are shown in Fig. 6.8 and the corresponding residuals are shown in Fig. 6.10.

To determine an appropriate dither range for a fixed number of Gaussians for a smooth potential with low RMS, it can be seen in Fig. 6.9 that a s/w_0 value of at least 0.11 and 0.05 over the entire pattern and the truncated region, respectively, should be used to simulate a smooth trapping potential with an RMS lying within a percent deviation from the best case trapping potential.
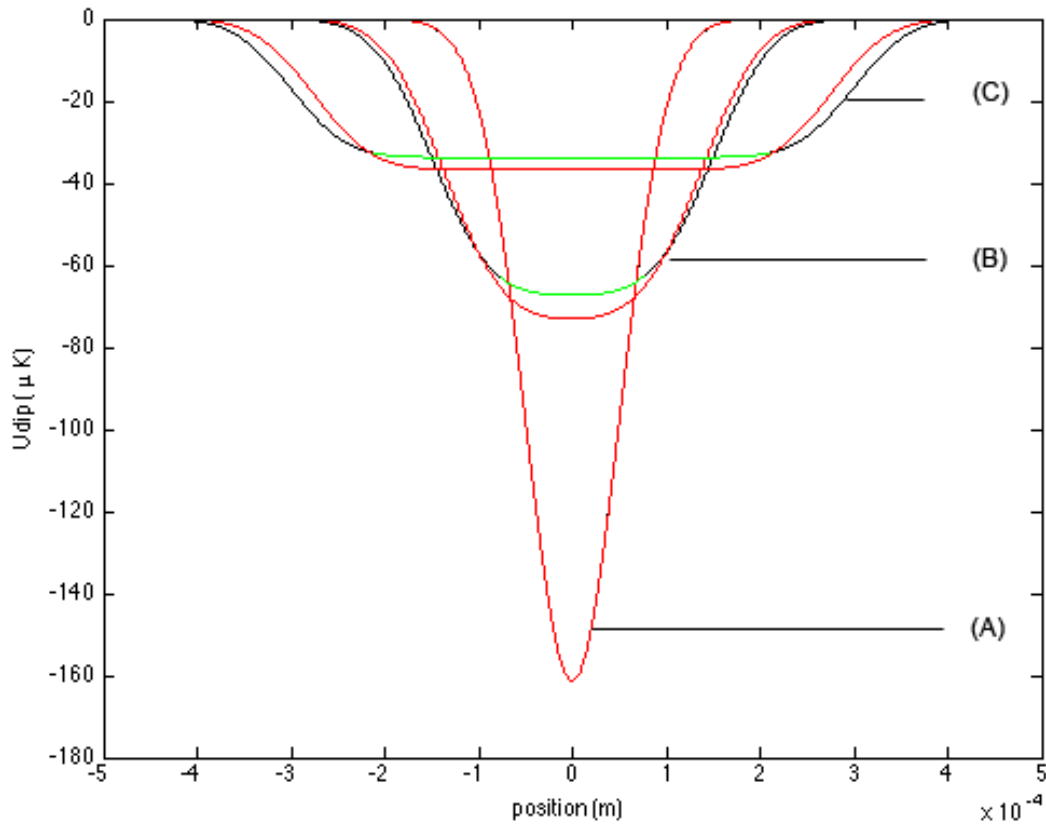
Figure 6.8: Trapping potential of the dithered beam (black) and the truncated region corresponding to a tenth of the total trap depth (green), and the best case trapping potential having 1200 Gaussians for each trapping potentials with different dither ranges (red). The best case potential plot for each dither range changes since unlike the previous case, the dither range was set a free parameter. Label (A)-(C) correspond to a s/w_0 value of 0.0083, 0.2500, and 0.5000, respectively.
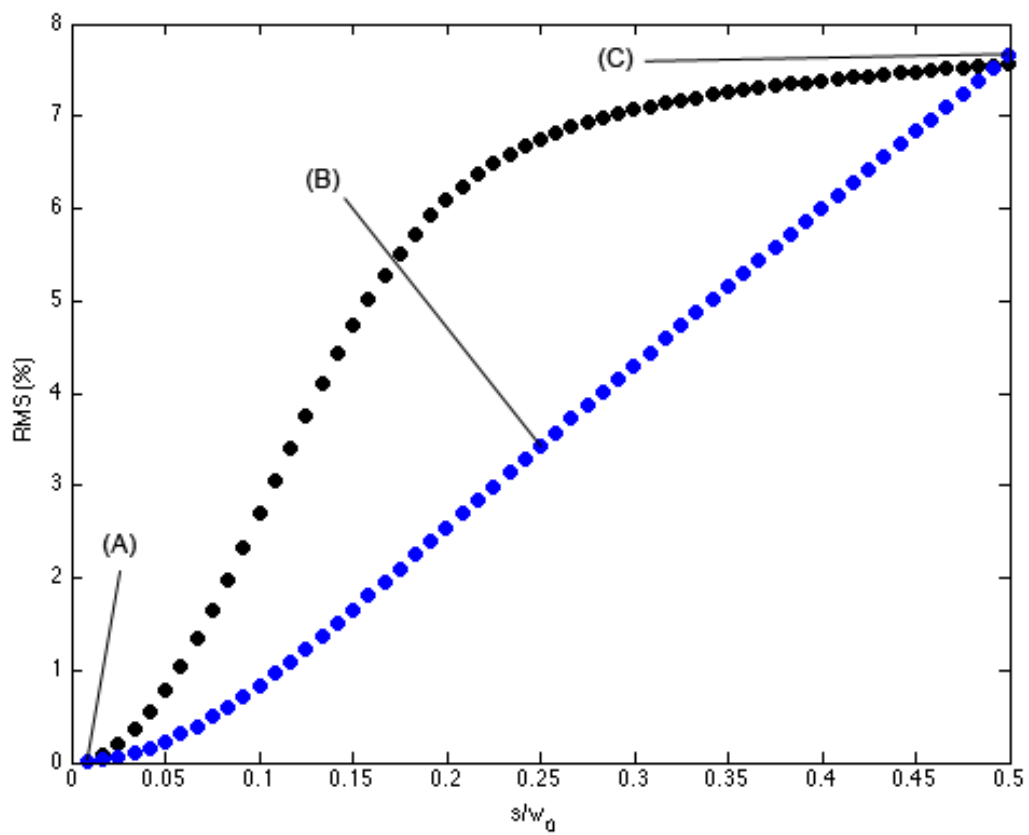
Figure 6.9: RMS across the entire pattern (black) and a tenth of the total trap depth (blue) of a dithered potential with the dither range set as a free parameter. Note: labels (A)-(C) correspond to plots (A)-(C) in Fig. 6.8.

(a)

(b)

(c)
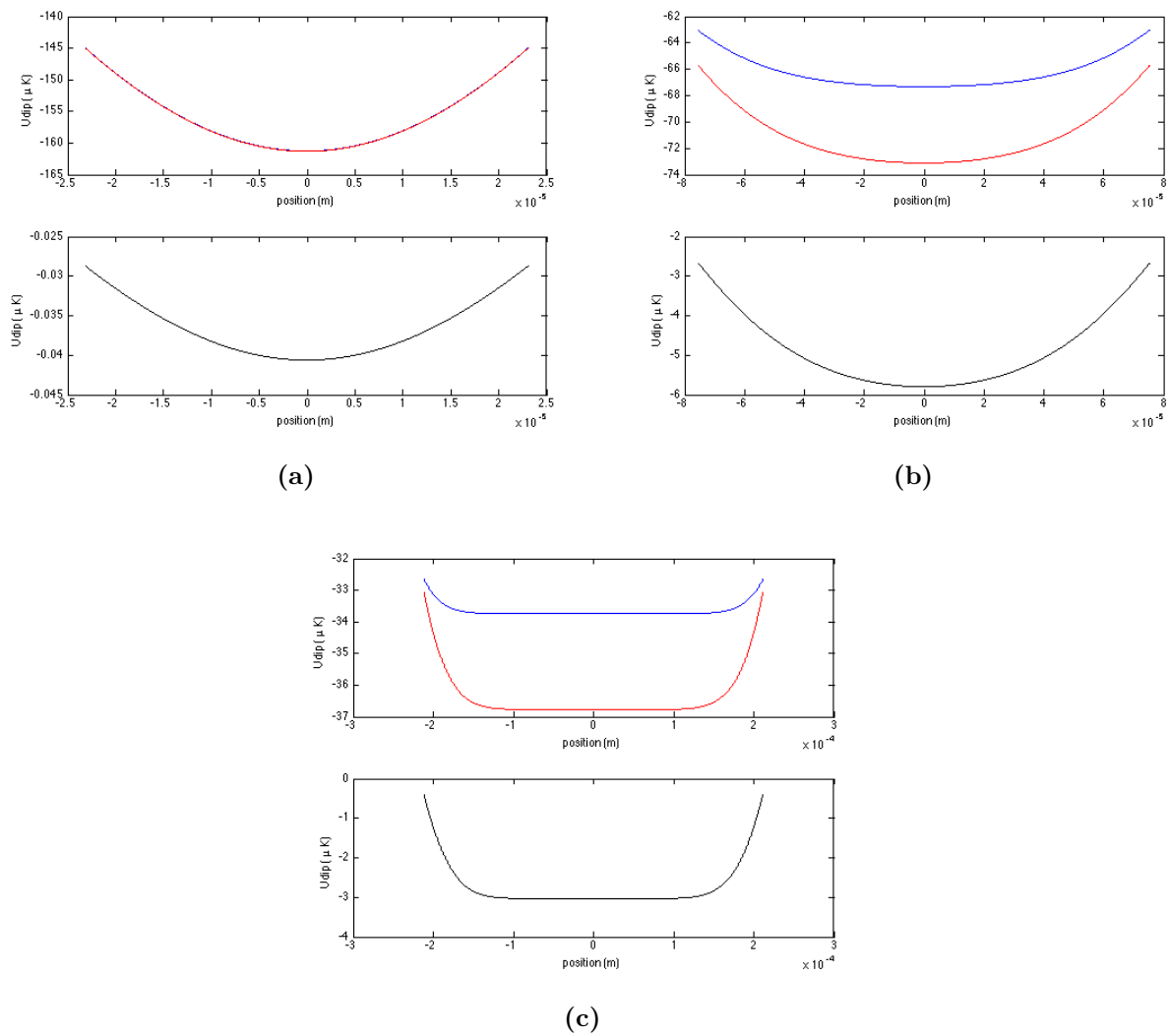
Figure 6.10: The top subplot of (a)-(c) show the trapping potential of the truncated region (blue) and the best case potential having 1101 Gaussians (red). The bottom subplot show the residuals corresponding to plots (A)-(C) in Fig. 6.8.

Chapter 7

Results

7.1 Trap Depth and Trapping Frequency

In this chapter, we characterise a simple harmonic potential, and determine a fitting distance over which accurate trapping frequency calculations can be made. This provides information in the experimental setting involving harmonic trap potentials where an accurate knowledge of the trap frequency is desired. Here, we characterise two quantities of interest: the depth of the trapping potential and the trap frequency.

We investigate the dependence of the trap depth on the dither range that is chosen. The dither range chosen for this purpose ranges from 0.1 times the beam waist to approximately 10 times the beam waist, which is set to 100 μm throughout part 2 of this report. The potential plots with these dither ranges are shown in Fig. 7.1, and the trap depth variation as a function of the dither range is seen in Fig. 7.2. In this case, since the free parameter is set to be the dither range, all trapping potentials have the same number of Gaussians. As expected, the trap depth decreases as the dither range is increased. Since the constituent Gaussians are summed over a bigger distance, the step size is larger for a bigger dither range and this results in a shallower potential, as it can be seen from (A)-(C) in Figs. 7.1 and 7.2.

All plots are made dimensionless by dividing the minimum of the dithered trap potential, U, by the minimum of the undithered Gaussian potential, U_0, or by dividing the undithered trap frequency calculated from a specific trap depth ω_0 by the trap frequency for different dither ranges over the same trap depth, ω. The x-axis is made dimensionless by dividing the dither range, A, by the beam waist, w_0, which is set to 100 μm for convenience. By making the plots dimensionless in such a way, the results may be applied across different experimental systems if the ratio A/w_0 is known. In Figs. 7.1 and 7.4,

the position coordinate (μm) is made dimensionless by dividing by w_0 and the potential U_{dip} (μK) normalised to U_0 to easily observe the effect of dithering on the potential trap depth.
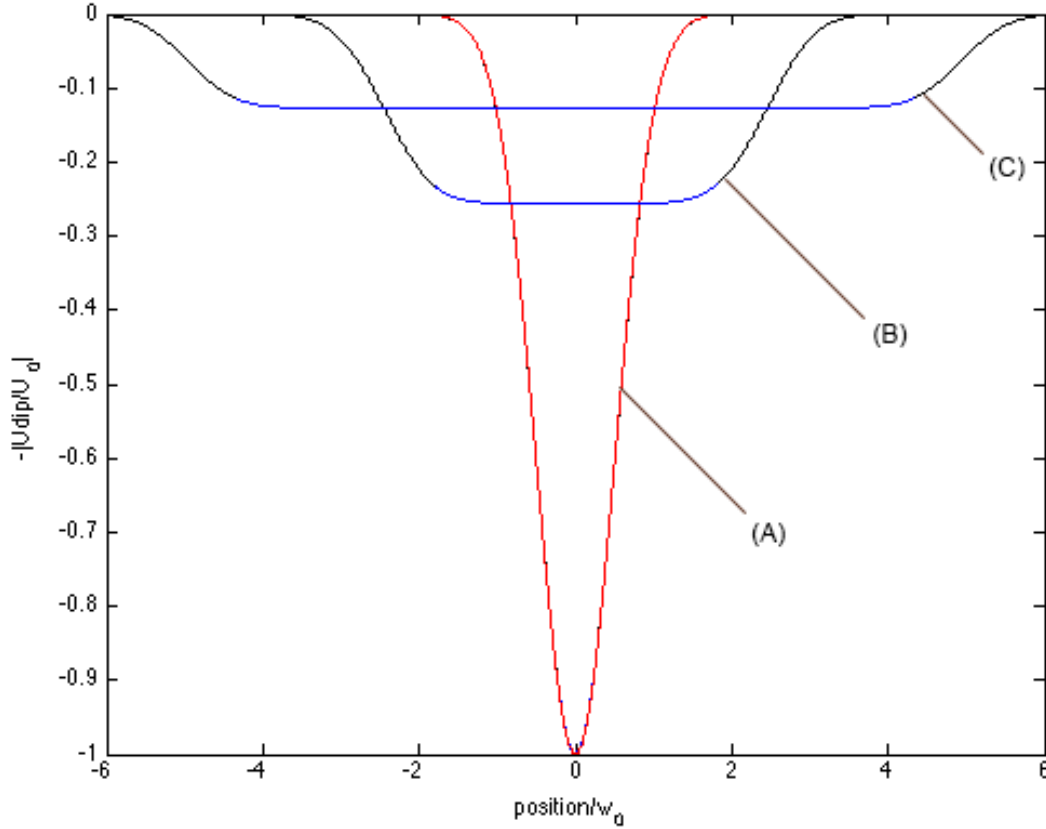
**Figure 7.1:** Trapping potential plots showing the dithered potentials with different dither ranges (black), the truncated region corresponding to a tenth of the total trap depth (blue) and the undithered beam (red) which closely overlaps with the smallest dither range with almost no dither. The plots are normalised by dividing the potential (U_{dip})by the minimum trap depth of the undithered potential, U_0. The beam waist is set to 100 μm. (A)-(C) correspond to an A/w_0 value of 0.1, 4.9, and 9.9, respectively.

The trapping frequencies of the dithered trap are found by performing a second order polynomial fit to the truncated region, corresponding to a tenth of the total trap depth defined in the previous chapter. The calculated frequency resulting from the fits to the trapping potentials and the residuals for select dither ranges are shown in Figs. 7.3 and 7.4, respectively. It is clear from the residual plots in Fig. 7.4 that an appropriate fitting region must be chosen to ensure an accurate frequency calculation from the harmonic fits for a particular dither range. To accurately calculate the frequency of the trapping potential, the region of the potential where the fitting is performed is redefined in terms of distance rather than range, since an accurate fit can only be performed for a fraction
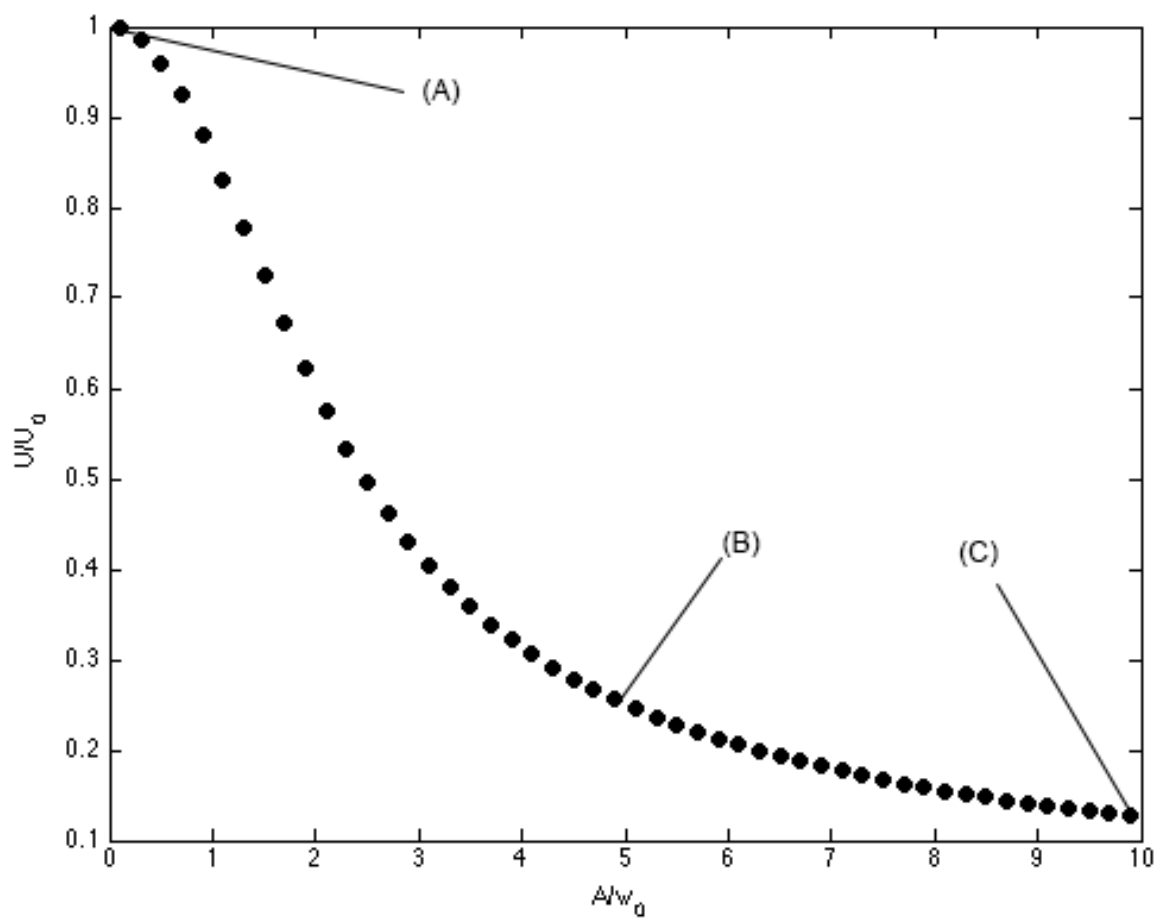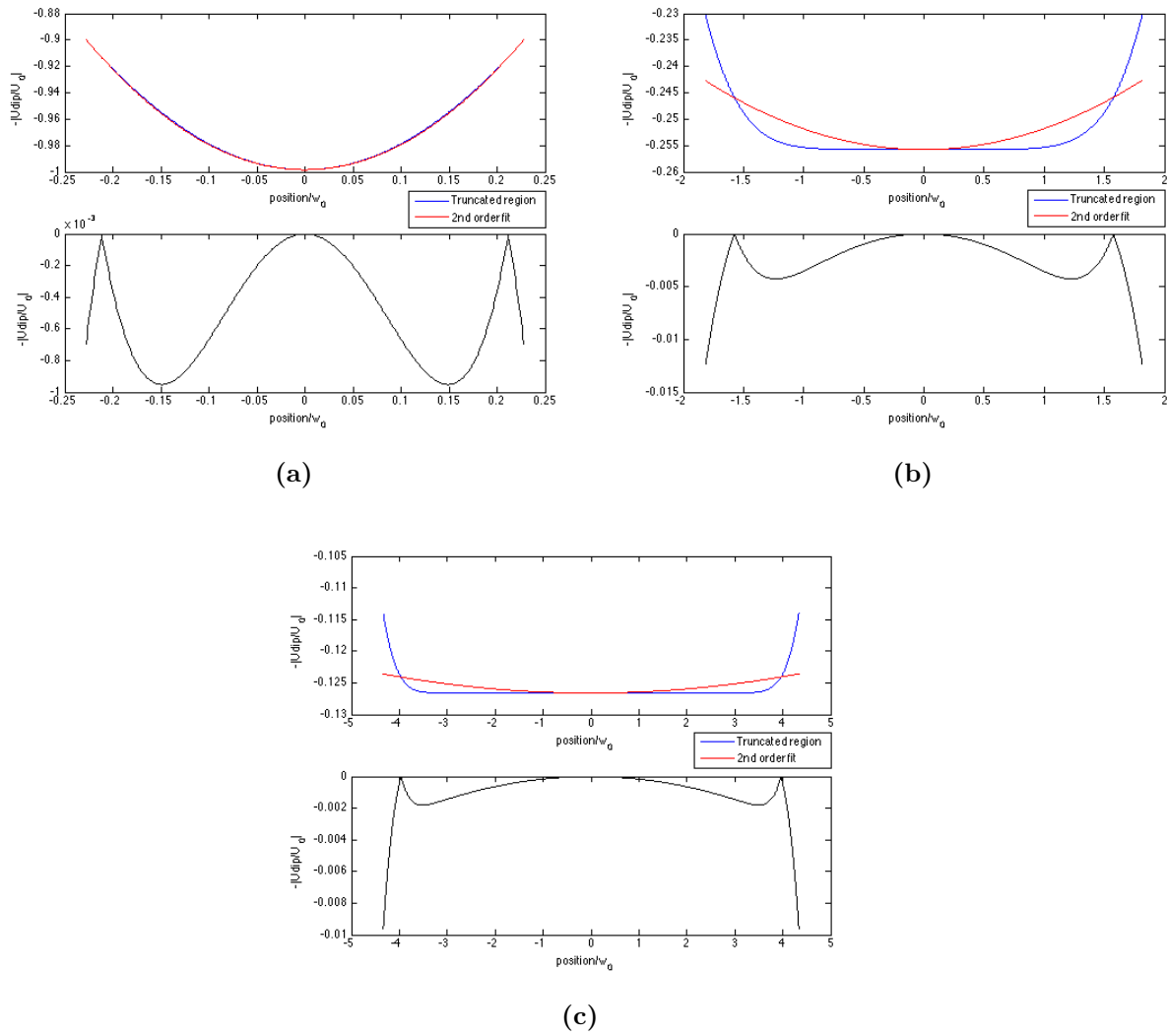
Figure 7.2: U/U_0 vs. A/w_0 where A is the dither range, w_0 is the beam waist, U is the minimum trap depth of the dithered trapping potential and U_0 is the minimum trap depth of the undithered potential. (A)-(C) correspond to an A/w_0 value of 0.1, 4.9, and 9.9, respectively. Note: labels (A)-(C) correspond to potentials (A)-(C) in Fig. 7.1.

of the beam waist and this is much smaller than the range that can be defined. This is illustrated in Fig. 7.5, which shows how the fitting distance corresponding to the range of the truncated region varies as a function of the dither range. The crossing point indicates the fitting distance when the dither range is equal to w_0. We take the trapping potential with the smallest dither range ($0.1w_0$) corresponding to (A) in Figs. 7.1 to 7.4 to determine the appropriate fitting distance δ for an accurate frequency calculation.
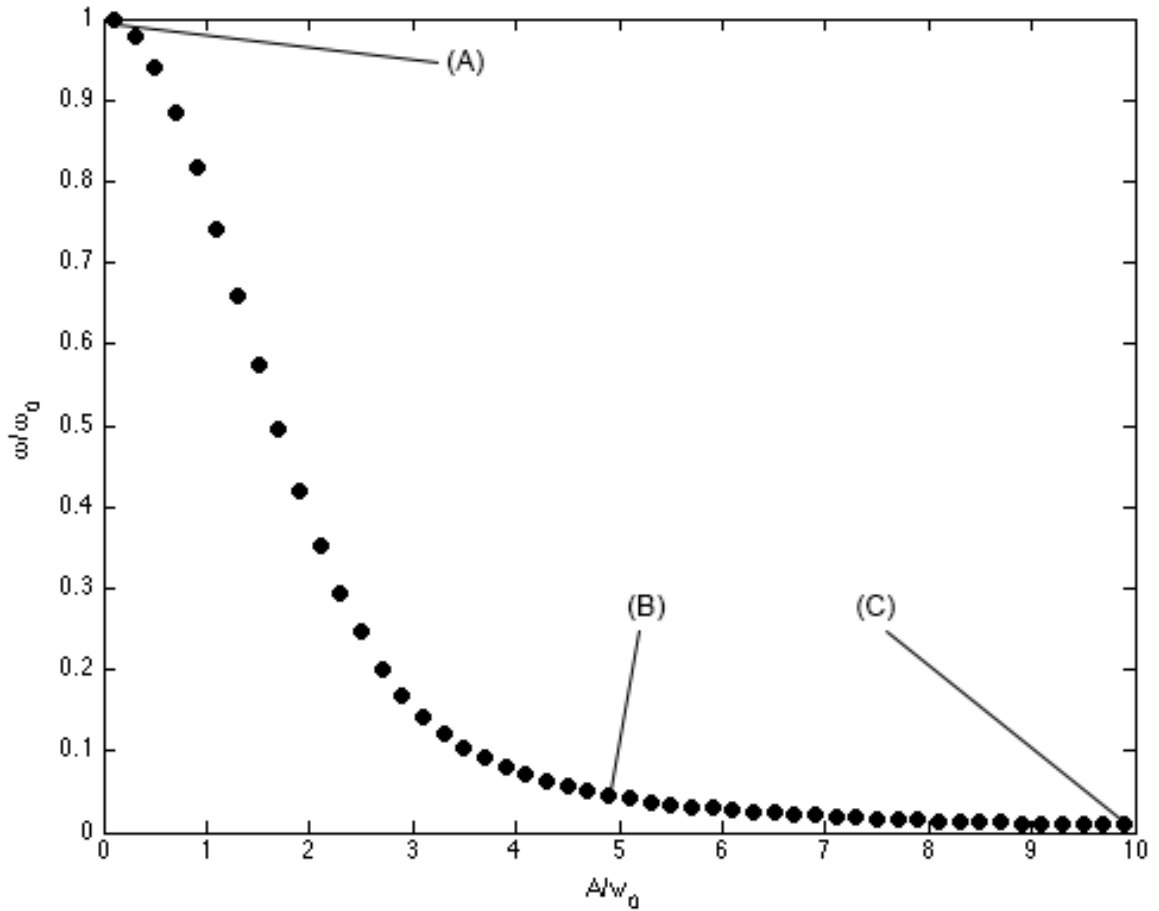
Figure 7.3: ω/ω_0 vs. A/w_0 where A is the dither range w_0 is the beam waist, ω is the frequency calculation from a second order polynomial fit for the dithered Gaussian, and ω_0 is the frequency resulting from a second order polynomial fit to the undithered Gaussian for a tenth of the total trap depth. (A)-(C) correspond to an A/w_0 value of 0.1,4.9, and 9.9, respectively. Note: labels (A)-(C) correspond to labels (A)-(C) in Figs. 7.1 and 7.2.

For a dither range of $0.1w_0$, we plot the calculated frequency using a second order polynomial fit across a range of fitting distances on a semilog plot (Fig. 7.6). The fit distance used in the code ranges from 0.4% of the beam waist to 70% of the beam waist. The value of the constant frequency, ω_0 can be found found analytically by expansion of the exponential term of a Gaussian, giving 2514.6. The frequency obtained from the calcu-

(a)

(b)

(c)

Figure 7.4: The top subplot shows the truncated distance corresponding to a tenth of the total trap depth (blue) and the second order polynomial fit to the dither range (red). A/w_0 values for (A)-(C) are 0.1, 4.9, and 9.9, respectively.
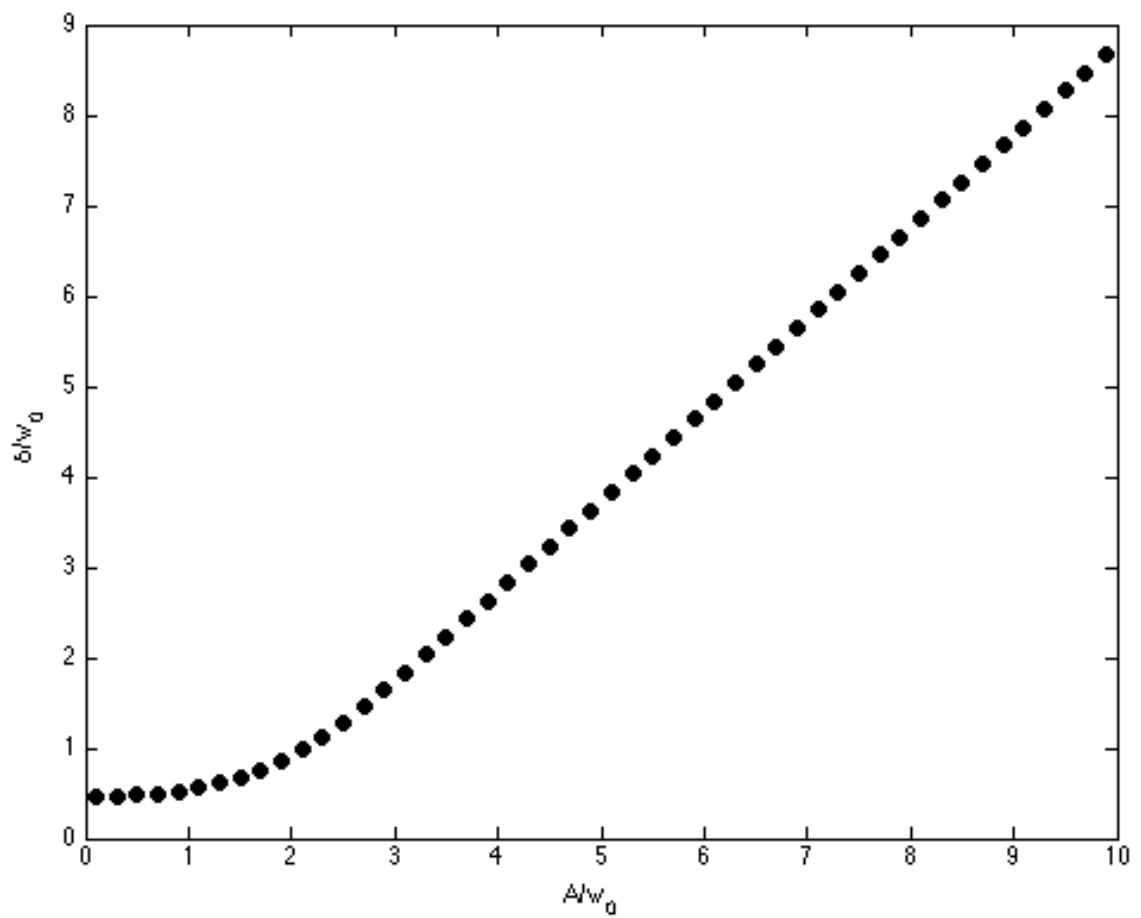
Figure 7.5: δ/w_0 vs. A/w_0 where A is the dither range, w_0 is the beam waist, and δ is the fitting distance over a tenth of the total trap depth. The value of δ as a fraction of the beam waist is 0.458.

lated fit is compared to the analytical expansion and found to be within 1% difference, attributable to numeric error. A fit distance which gives a frequency calculation that lies within a percent deviation from the analytic trap frequency is seen to be less than 30% of the beam waist.

To show the degree of deviation from ω_0 as the fitting distance is increased, the percent deviation from this analytical value is plotted in Fig. 7.7. For the maximal fit distance, a single Gaussian suffices for an RMS deviation of 0.17% from a best case trapping potential consisting of 1001 Gaussians, as seen in Fig. 7.8. The residuals for the select fitting distances in Figs. 7.6 and 7.7 are seen in Fig. 7.9.
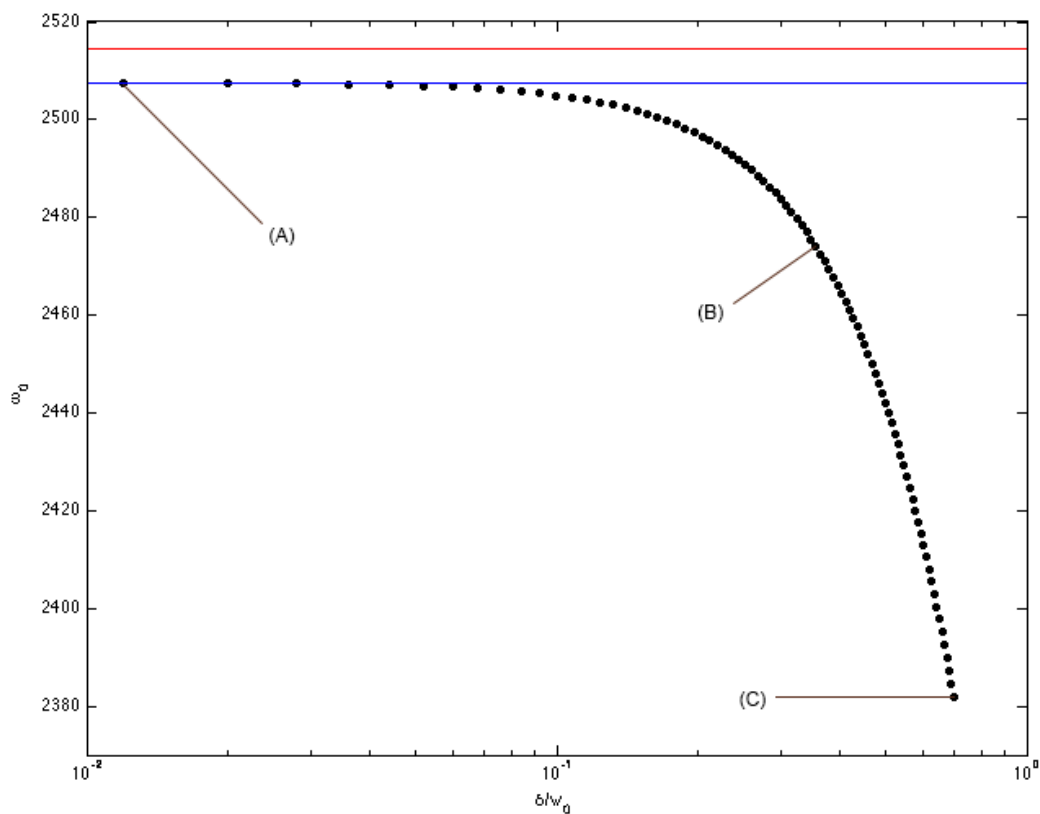
Figure 7.6: ω_0 vs. δ/w_0 where δ is the distance over which the fit is performed, w_0 is the beam waist, ω is the frequency over the corresponding distance of fitting δ. The red line indicates the analytical value of ω_0 and the blue line is the calculated value of ω_0. The fit range for which the variation from the calculated value of the maximum frequency lies within a percent is between 0.006 and 0.3.
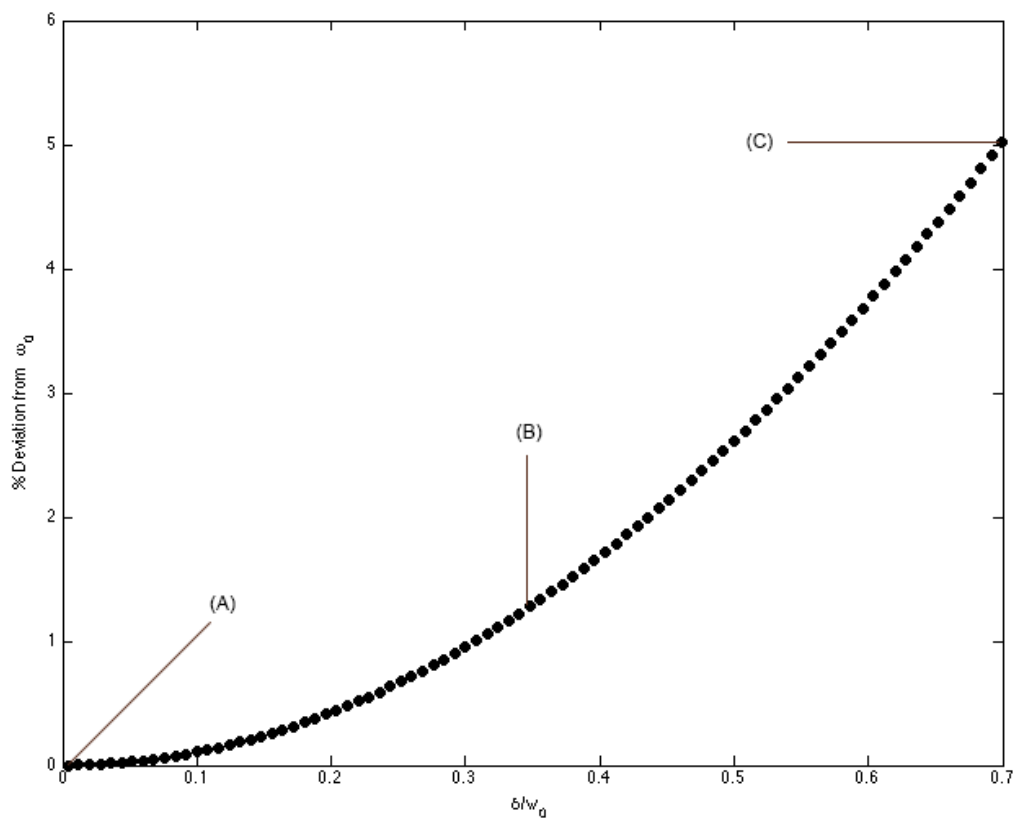
Figure 7.7: Percent deviation from the calculated value of ω_0 vs. δ/ω_0 where δ is the fitting distance which is proportional to the trap depth over which the fitting routine is performed and w_0 is the beam waist. The fit range for which the variation from the calculated value of the maximum frequency lies within a percent is between 0.006 and 0.3.
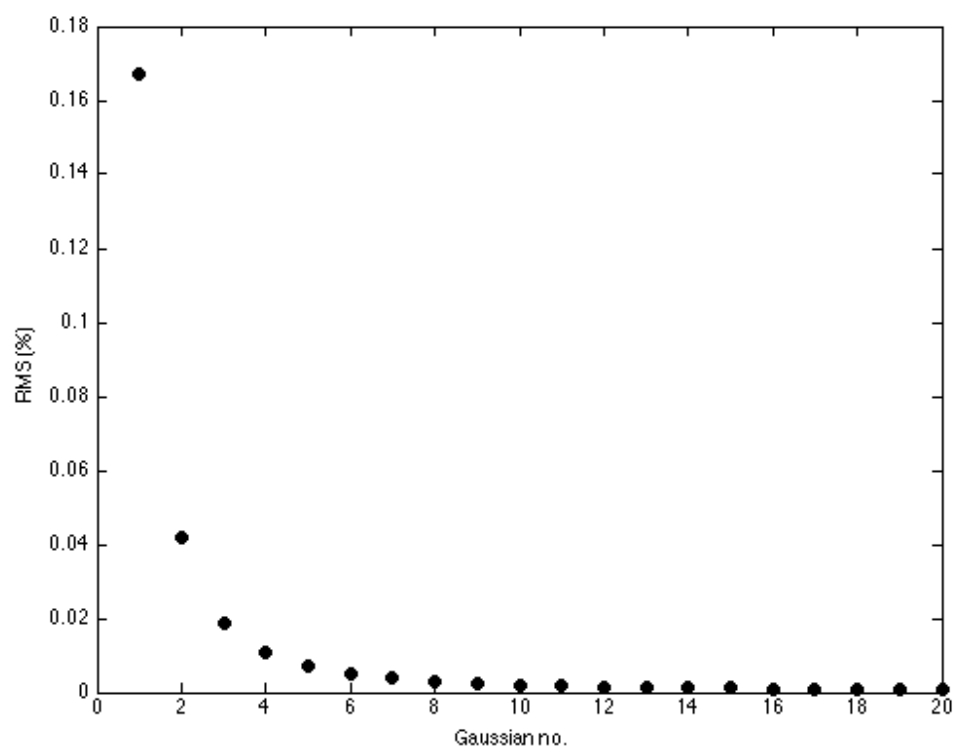
Figure 7.8: RMS deviation vs. number of Gaussians in percentage from a best case trapping potential consisting of 1001 Gaussians. For a small dither range which is 10% of the beam waist, a single Gaussian suffices for a small RMS deviation of 0.17% from the best case potential.

(a)

(b)

(c)
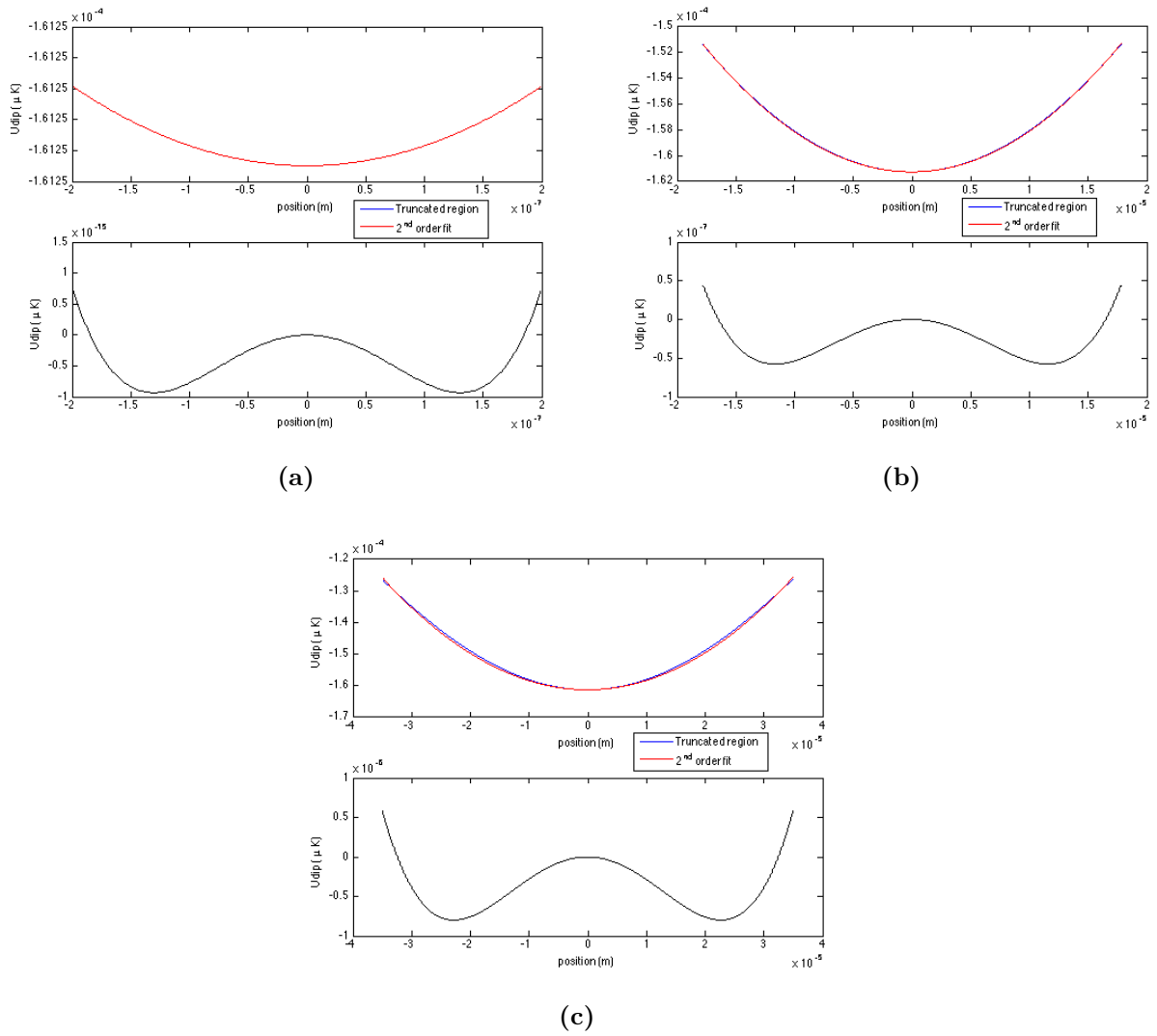
Figure 7.9: The top subplots (a)-(c) show the trapping potentials for different fit distances (blue) and the second order polynomial fits to the fit distances. Plots (a)-(c) correspond to (A)-(C) in Figs. 7.6 and 7.7. The fit distance as a fraction of the beam waist (δ/w_0) and the frequency calculation from the fits are (a) 0.004, 2.51 kHz (b) 0.36, 2.47 kHz and (c) 0.7, 2.38 kHz

Chapter 8

Conclusion

In part 1 of the report, we have investigated the D2 lines of a mixture cell containing natural abundance cesium and potassium. It was found that the mixture species cell behaves independently of each other for temperatures up to approximately 150 °C for the K D2 line. Above the temperature of 155 °C, the spectroscopic signal from the K D2 line was found to exhibit absorption features on the wings of the Doppler broadened transmission spectrum. These absorption features are not the product of any transitions of the K D2 line and the vibrational transitions are orders of magnitude bigger compared to the frequency, while the rotational transition is comparable in terms of the order of magnitude suggested in literature, suggesting that these features may potentially be the result of rotational transitions in the K2 molecule. Futher experimental work to better characterise these features was prevented due to the alkaline metals reacting with the pyrex glass at these high temperatures, however, these features from the spectroscopic signals provide an interesting starting point for future investigations. In part 2 of the report, we developed codes on MATLAB simulating time-averaged potentials. We presented three different coding methods to simulate time-averaged optical potentials and determined the step sizes necessary to reproduce a smooth trapping potential with low RMS errors of less than one percent. We also presented the results from characterising the depth of a harmonic trapping potential and determined the distance over which the frequency of a trapping potential can be fitted accurately. Such information may be desirable for experiments involving trapping BECs in a harmonic potentials where an accurate chracterisation of the trap frequency is required.

Bibliography

[1] P. Siddons, C. S. Adams, C. Ge, and I. G. Hughes, *Absolute absorption on rubidium D lines: comparison between theory and experiment*, Journal of Physics B: Atomic, Molecular and Optical Physics **41**, 155004 (2008).

[2] K. Henderson, C. Ryu, C. MacCormick, and M. Boshier, *Experimental demonstration of painting arbitrary and dynamic potentials for Bose–Einstein condensates*, New Journal of Physics **11**, 043030 (2009).

[3] A. L. Gaunt, T. F. Schmidutz, I. Gotlibovych, R. P. Smith, and Z. Hadzibabic, *Bose-Einstein condensation of atoms in a uniform potential*, Physical Review Letters **110**, 200406 (2013).

[4] G. D. Bruce, S. L. Bromley, G. Smirne, L. Torralbo-Campo, and D. Cassettari, *Holographic power-law traps for the efficient production of Bose-Einstein condensates*, Physical Review A **84**, 053410 (2011).

[5] F. Fatemi, M. Bashkansky, and Z. Dutton, *Dynamic high-speed spatial manipulation of cold atoms using acousto-optic and spatial light modulation*, Optics express **15**, 3589 (2007).

[6] N. V. Tkachenko, *Optical spectroscopy: methods and instrumentations* (Elsevier, 2006).

[7] O. Svelto and D. C. Hanna, *Principles of lasers* (Springer, 1976).

[8] J. Keaveney, *Collective Atom-Light Interactions in Dense Atomic Vapours* (Springer, 2014).

[9] D. Suter, *The physics of laser-atom interactions* volume 19 (Cambridge University Press, 1997).

[10] D. A. Steck, *Cesium D line data*, Los Alamos National Laboratory (unpublished) **124** (2003).

[11] T. Tiecke, *Properties of potassium*, University of Amsterdam, The Netherlands, Thesis (2010).

[12] M. A. Zentile *et al.*, *ElecSus: A program to calculate the electric susceptibility of an atomic ensemble*, Computer Physics Communications **189**, 162 (2015).

[13] M. I. Lourakis, *A brief description of the Levenberg-Marquardt algorithm implemented*

by levmar, Foundation of Research and Technology **4**, 1 (2005).

[14] C. Alcock, V. Itkin, and M. Horrigan, *Vapour pressure equations for the metallic elements: 298–2500K*, Canadian Metallurgical Quarterly **23**, 309 (1984).

[15] B. E. Sherlock and I. G. Hughes, *How weak is a weak probe in laser spectroscopy?*, American Journal of Physics **77**, 111 (2009).

[16] W. J. Tango, J. K. Link, and R. N. Zare, *Spectroscopy of K2 Using Laser-Induced Fluorescence*, The Journal of Chemical Physics **49**, 4264 (1968).

[17] H. Wang, P. Gould, and W. Stwalley, *Photoassociative spectroscopy of ultracold K 39 atoms in a high-density vapor-cell magneto-optical trap*, Physical Review A **53**, R1216 (1996).

[18] D. R. Pape, A. P. Goutzoulis, and S. V. Kulakov, *Design and fabrication of acousto-optic devices* (M. Dekker, 1994).

[19] N. J. Berg and J. N. Lee, *Acousto-optic signal processing: theory and implementation*, in *New York, Marcel Dekker, Inc.(Optical Engineering. Volume 2), 1983, 496 p. No individual items are abstracted in this volume.*, volume 2, 1983.

[20] F. Träger, *Springer handbook of lasers and optics* (Springer Science & Business Media, 2007).

[21] R. Grimm, M. Weidemüller, and Y. B. Ovchinnikov, *Optical dipole traps for neutral atoms*, Advances in atomic, molecular, and optical physics **42**, 95 (2000).

[22] D. Trypogeorgos, T. Harte, A. Bonnin, and C. Foot, *Precise shaping of laser light by an acousto-optic deflector*, Optics express **21**, 24837 (2013).

[23] M. Pasienski and B. DeMarco, *A high-accuracy algorithm for designing arbitrary holographic atom traps*, Optics express **16**, 2176 (2008).

Part III

Appendices

Appendix A

Properties of Cs D2 and K D2 Transitions

Quantity	Symbol	Value
Atomic mass	m	2.206 946 50(17)$\times 10^{-25}$ kg
Melting point	$T_{m.p}$	28.44°C (301.59 K)
Frequency	$\eta/2\pi$	351.725 718 50(11) THz
Wavelength	λ	852.118 73 nm
Natural linewidth	$\Gamma_0/2\pi$	5.2227(66) MHz
Lifetime	τ	30.473(39) ns
Transition frequency	ω	$2\pi 351.72571850(11)$ THz
Saturation intensity	I_{sat}	2.71 mW/cm^2

Table A.1: Properties of natural abundance cesium [10]

Quantity	Symbol	Value
Atomic mass	m ^{39}K	38.963 706 68 u/6.470 080 128$\times 10^{-26}$ kg
Atomic mass	m ^{40}K	39.963 998 48(21) u/ 6.636 182 603$\times 10^{-26}$ kg
Atomic mass	m ^{41}K	40.961 825 76(21) u/6.801 875 834$\times 10^{-21}$ kg
Melting point	T$_{m.p}$	65.65°C (336.8 K)
Frequency	η	391.016 THz
Wavelength	λ	766.70 nm
Natural linewidth	$\Gamma_0/2\pi$	6.035(11) MHz
Lifetime	τ	26.37(5) ns
Transition frequency	ω	391.01617003(12) THz
Saturation intensity	I$_{sat}$	1.75 mW/cm^2

Table A.2: Properties of natural abundance K D2 line [11]

Appendix B

FWHM as a function of temperature for the ^{39}K D2 line
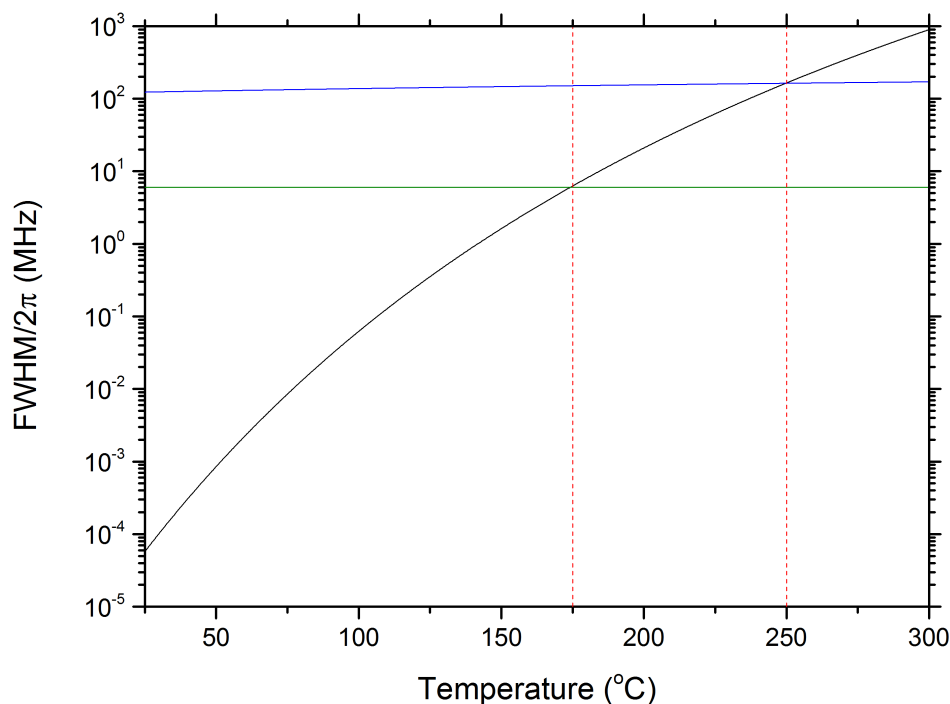
Figure B.1: FWHM of the Doppler (Γ_{D}), natural (Γ_0), and self-broadened (Γ_{self}) linewidths for the ^{39}K D2 line, shown in blue, dark green, and black, respectively. The dashed red lines indicate the boundaries separating different regimes where $\Gamma_{\mathrm{D}} > \Gamma_0 > \Gamma_{\mathrm{self}}$ between ~25 °C and ~175 °C, $\Gamma_{\mathrm{D}} > \Gamma_{\mathrm{self}} > \Gamma_0$ between ~175 °C and ~250 °C, and $\Gamma_{\mathrm{self}} > \Gamma_{\mathrm{D}} > \Gamma_0$ for temperatures greater than ~250 °C. Calculations of the linewidths are based on Refs.[1], [9].

Appendix C

Values

Quantity	Symbol	Value
Beam waist for waveguide	$w_{waveguide}$	102 μm
Beam waist for moving beam	w_{moving}	100 μm
Power in guide beam	P_{guide}	0 W
Power in moving beam	P_{moving}	20 W

Table C.1: Values used for the adjustable parameters

Quantity	Symbol	Value
Wavelength	λ	1070 nm
Transition wavelength	$\lambda_{resonance}$	780.2 nm
Atomic mass	m_{Rb}	$85 \times 1.661 \times 10^{-27}$ kg
Speed of light	c	3×10^{8} ms^{-1}
Natural linewidth	Γ	6.066 MHz
Boltzmann factor	k_B	1.381×10^{-23} J·K^{-1}
Reduced Plank's constant	$\hbar$	1.054×10^{-34} J·s

Table C.2: Values of constants

Appendix D

Code characterising the RMS error with the dither range set as a fixed parameter

All The Constants

```
wavelength = 1070e-9;    % nm
mass_Rb = 85*1.661e-27; % kg
res = 780.2e-9;         % Approximate Rb resonant wavelength (D2)
c = 3e8;                % Speed of light
angfreq = 2*pi*c/res;
detuning = (c/wavelength - c/res);
gamma = 6.0666e6;       % natural linewidth 85Rb in MHz (D2)
kB = 1.381e-23;
hbar = 1.054e-34;
```

Adjustable Parameters

```
% Beam parameters
waist_guide = 102e-6;   % beam waist for waveguide
waist_moving = 100e-6;  % beam waist for moving beam
rayleighLength_guide = pi*waist_guide^2/wavelength;
rayleighLength_moving = pi*waist_moving^2/wavelength;
Pguide = 0;             % power in guide beam
Pmoving = 20;           % power in moving beam (W)
```

```matlab
acceleration = 3;      % Choose!
```

1D Model

```matlab
rangeMax = 0.0005;
stepSize = 0.000001;
rr = -rangeMax:stepSize:rangeMax;
zz = 0;

ditherLength = 0.0005;
bestcasedither_range = -ditherLength/2:0.0000005:ditherLength/2;
gaussianNoMax=50;
ditherGaussArray = 4:2:gaussianNoMax;
disp('best case G no')
disp(length(bestcasedither_range))
ditherStepArraynorm = zeros(size(ditherGaussArray));

rmsflat = zeros(size(ditherGaussArray));
rmswhole = zeros(size(ditherGaussArray));
Stepsize = zeros(size(ditherGaussArray));

iter=1;

intensity_summed1 = zeros(size(rr));
```

best case potential

```matlab
for r_offsetbest = bestcasedither_range;
    intensity1D1 = intensity(rr - r_offsetbest,zz,Pmoving,
    rayleighLength_moving,waist_moving);
    intensity_summed1 = intensity_summed1 + intensity1D1;
end

intensity_normalised1 = intensity_summed1/length(bestcasedither_range);
Udip1Dbest = (3/2)*(pi*c^2/angfreq^3)*(gamma/detuning)*intensity_normalised1/kB;
```

```
for gaussianNum = ditherGaussArray;
    ditherMin=ditherLength/2*(1/gaussianNum-1);


    dither_range = ditherMin:ditherLength/gaussianNum:-ditherMin;
    %Set desired dithering amount (ditherMax matched to best case)


    intensity_summed = zeros(size(rr));


    for r_offset = dither_range
        intensity1D = intensity(rr - r_offset,zz,Pmoving,
        rayleighLength_moving,waist_moving);
        intensity_summed = intensity_summed + intensity1D;
    end


    intensity_normalised = intensity_summed/length(dither_range);


    Udip1D = (3/2)*(pi*c^2/angfreq^3)*(gamma/detuning)*intensity_normalised/kB;


    ditherStepArraynorm(iter)=ditherLength/gaussianNum/waist_moving;
    Stepsize(iter) = ditherLength/gaussianNum;

%%%%%%%%%%%%%%%%%%%%%%%%%%%%%%%%%%%%%%%%%%%%%%%

    Udip1DbestNorm=Udip1Dbest./(Udip1Dbest(round(length(rr)/2)));
    ratio = 0;
    trim = 0;
    tolerance =0.001;
    trimRatio = 9/10;


    while ratio< (trimRatio-tolerance)
        trim=trim+1;
        ratio = Udip1DbestNorm(trim);
    end


    intensity_summed = zeros(size(rr));


    for r_offset = dither_range
```

```
        intensity1D = intensity(rr - r_offset,zz,Pmoving,
        rayleighLength_moving,waist_moving);
        intensity_summed = intensity_summed + intensity1D;
    end



    trimArbitrary = trim;
    rrTruncate = rr(trimArbitrary+1:(length(rr)-trimArbitrary));
    UdipTruncateArbitrary = Udip1D(trimArbitrary+1:(length(rr)-trimArbitrary));
    Udip1DbestTrunc = Udip1Dbest(trimArbitrary+1:(length(rr)-trimArbitrary));
    %Truncate Udip1D bestcase to flat region only



%%RMS calculation
    RMS = -sqrt((sum((Udip1D-Udip1Dbest).^2)/length(Udip1D)))/min(Udip1Dbest)*100;
    %RMS across whole pattern

    RMSflat = -sqrt(sum((UdipTruncateArbitrary-Udip1DbestTrunc).^2)/
    length(UdipTruncateArbitrary))/min(Udip1Dbest)*100; %RMS over truncated region on

    rmswhole(iter)=RMS;
    rmsflat(iter)=RMSflat;

    Residuals = UdipTruncateArbitrary-Udip1DbestTrunc;

    if iter ==1

    figure(1)
    plot(rr,Udip1D,'k')
    hold on
    plot(rrTruncate,UdipTruncateArbitrary,'g')
    hold on

    figure(2)
    subplot(2,1,1);
    plot(rrTruncate,UdipTruncateArbitrary,'b')
    hold on
```

```
plot(rrTruncate,Udip1DbestTrunc,'r')
xlabel('position (m)')
ylabel('Udip (\muK)')
legend('Truncated region','Best case')
%set(gca,'FontSize',14)
%title(' plots for Truncated Region (blue) and polynomial fit (red)')
subplot(2,1,2);
plot(rrTruncate,Residuals,'k')
%hold on
%plot(rrTruncate,line,'b')
xlabel('position (m)')
%set(gca,'FontSize',14)
ylabel('Udip (\muK)')
%set(gca,'FontSize',14)

disp('res1iter')
disp(iter)
disp('Gno1')
disp(ditherGaussArray(iter))
disp('stepsize1')
disp(Stepsize(iter))
disp('stepsize/BW1')
disp(ditherStepArraynorm(iter))
hold off
end

if iter ==3
figure(1)
plot(rr,Udip1D,'k')
hold on
plot(rrTruncate,UdipTruncateArbitrary,'g')
hold on

figure(3)
subplot(2,1,1);
plot(rrTruncate,UdipTruncateArbitrary,'b')
hold on
```

```
plot(rrTruncate,Udip1DbestTrunc,'r')
legend('Truncated region','Best case')
xlabel('position (m)')
%set(gca,'FontSize',14)
ylabel('Udip (\muK)')
%set(gca,'FontSize',14)
%title(' plots for Truncated Region (blue) and polynomial fit (red)')
subplot(2,1,2);
plot(rrTruncate,Residuals,'k')
%title('Residuals')
xlabel('position (m)')
ylabel('Udip (\muK)')

disp('res2iter')
disp(iter)
disp('Gno2')
disp(ditherGaussArray(iter))
disp('stepsize2')
disp(Stepsize(iter))
disp('stepsize/BW2')
disp(ditherStepArraynorm(iter))

hold off
end

if iter ==24
figure(1)
plot(rr,Udip1D,'k')
hold on
plot(rr,Udip1Dbest,'r')
hold on
plot(rrTruncate,UdipTruncateArbitrary,'g')
xlabel('position (m)')
ylabel('Udip (\muK)')
hold on

figure(4)
```

```
    subplot(2,1,1);
    plot(rrTruncate,UdipTruncateArbitrary,'b')
    hold on
    plot(rrTruncate,Udip1DbestTrunc,'r')
    legend('Truncated region','Best case')
    xlabel('position (m)')
    %set(gca,'FontSize',14)
    ylabel('Udip (\muK)')
    %set(gca,'FontSize',14)
    %title(' plots for Truncated Region (blue) and polynomial fit (red)')
    subplot(2,1,2);
    plot(rrTruncate,Residuals,'k')
    %title('Residuals')
    xlabel('position (m)')
    %set(gca,'FontSize',14)
    ylabel('Udip (\muK)')
    %set(gca,'FontSize',14)
    hold off

    disp('res3iter')
    disp(iter)
    disp('Gno3')
    disp(ditherGaussArray(iter))
    disp('stepsize3')
    disp(Stepsize(iter))
    disp('stepsize/BW3')
    disp(ditherStepArraynorm(iter))
    end

    iter=iter+1;


end

hold off

disp('maxiter')
```

```
disp(iter)

figure(5)
scatter(ditherStepArraynorm,rmswhole,'filled','k')
hold on
scatter(ditherStepArraynorm,rmsflat,'filled','b')
hold off
box on
xlabel('Step Size/beam waist')
ylabel('RMS (%)')

figure(6)
semilogx(ditherStepArraynorm,rmswhole,'ok',
'MarkerEdgeColor','k','MarkerFaceColor','k','MarkerSize',5)
hold on
semilogx(ditherStepArraynorm,rmsflat,'ob',
'MarkerEdgeColor','b','MarkerFaceColor','b','MarkerSize',5)
axis([0,2,0,7])
box on
xlabel('Step Size/beam waist')
ylabel('RMS (%)')
legend('RMS across whole pattern','RMS over truncated region')
```